



UNIVERSIDADE ESTADUAL DE CAMPINAS
Instituto de Física Gleb Wataghin

Larissa Helena Mendes

**Simulating Hexagonal Pixel Designs for Monolithic
Active Pixel Sensors**

Simulação de Designs de Pixeis Hexagonais para Sensor
Monolítico de Pixel Ativo

Campinas
2023

Larissa Helena Mendes

**Simulating Hexagonal Pixel Designs for Monolithic Active Pixel
Sensors**

Simulação de Designs de Pixeis Hexagonais para Sensor Monolítico de Pixel
Ativo

Thesis presented to the *Gleb Wataghin* Institute of Physics of the University of Campinas in partial fulfillment of the requirements for the degree of Master in Physics in Computer Science, in the area of Applied Physics.

Dissertação apresentada ao Instituto de Física *Gleb Wataghin* da Universidade Estadual de Campinas como parte dos requisitos para a obtenção do título de Mestra em Física, na área de Física Aplicada.

Supervisor/Orientadora: Profa. Dra. Alessandra Tomal
Co-supervisor/ Coorientador: Dr. Simon Spannagel

Este trabalho corresponde à versão final da Dissertação defendida por Larissa Helena Mendes e orientada pela Profa. Dra. Alessandra Tomal.

Campinas
2023

Ficha catalográfica
Universidade Estadual de Campinas
Biblioteca do Instituto de Física Gleb Wataghin
Lucimeire de Oliveira Silva da Rocha - CRB 8/9174

M522s Mendes, Larissa Helena, 1996-
Simulating hexagonal pixel designs for monolithic active pixel sensors /
Larissa Helena Mendes. – Campinas, SP : [s.n.], 2023.

Orientador: Alessandra Tomal.
Coorientador: Simon Spannagel.
Dissertação (mestrado) – Universidade Estadual de Campinas, Instituto de Física Gleb Wataghin.

1. Silício. 2. Método de Monte Carlo. 3. Detectores - Métodos de simulação. I. Tomal, Alessandra, 1983-. II. Spannagel, Simon. III. Universidade Estadual de Campinas. Instituto de Física Gleb Wataghin. IV. Título.

Informações Complementares

Título em outro idioma: Simulação de designs de pixels hexagonais para sensor monolítico de pixel ativo

Palavras-chave em inglês:

Silicon

Monte Carlo method

Detectors - Simulation methods

Área de concentração: Física Aplicada

Titulação: Mestra em Física

Banca examinadora:

Alessandra Tomal [Orientador]

Ana Amélia Bergamini Machado

Ingrid Maria Gregor

Data de defesa: 26-04-2023

Programa de Pós-Graduação: Física

Identificação e informações acadêmicas do(a) aluno(a)

- ORCID do autor: <https://orcid.org/0000-0002-5481-7804>

- Currículo Lattes do autor: <http://lattes.cnpq.br/8834772761967018>



INSTITUTO DE FÍSICA
GLEB WATAGHIN

MEMBROS DA COMISSÃO EXAMINADORA DA DISSERTAÇÃO DE MESTRADO DA ALUNA LARISSA HELENA MENDES - RA 231494 APRESENTADA E APROVADA AO INSTITUTO DE FÍSICA GLEB WATAGHIN, DA UNIVERSIDADE ESTADUAL DE CAMPINAS, EM 26/04/2023.

COMISSÃO JULGADORA:

- Profa. Dra. Alessandra Tomal - Presidente e orientadora (IFGW/UNICAMP)
- Profa. Dra. Ana Amélia Bergamini Machado (IFGW/UNICAMP)
- Profa. Dra. Ingrid Maria Gregor (Deutsches Elektronen-Synchrotron)

OBS.: Ata da defesa com as respectivas assinaturas dos membros encontra-se no SIGA/Sistema de Fluxo de Dissertação/Tese e na Secretaria do Programa da Unidade.

CAMPINAS

2023

Acknowledgements

I would like to express my gratitude to everyone who has supported and guided me throughout my research journey in completing this thesis.

First and foremost, I would like to express my sincere gratitude to my supervisors Prof. Dr. Alessandra Tomal and Dr. Simon Spannagel for their guidance and support throughout this research project. Alessandra's expertise and insightful feedbacks were instrumental in shaping the direction of my research, and Simon's supervision allowed me to work on an exciting topic and gain valuable knowledge and skills.

I am also grateful to the individuals who have supported and collaborated with me as part of the Tangerine project at the ATLAS-DESY group. Thank you to Adriana, Gianpiero, Sara, Manuel, Nastya, Simon, Håkan, Lennart, Paul, Naomi, Daniil, Finn, and Stephan. I appreciate their warm and supportive nature, which has created an ideal working environment. Even though I was working from distance, the welcoming nature of the group and institution made me feel part of the team. Special thanks to Håkan Wennlöf for his collaboration and support with the Allpix² simulations and insightful discussions.

I would like to extend my sincere gratitude to the thesis referees for their invaluable feedback and suggestions, which have helped me to improve the quality of this thesis.

Finally, I would like to express my appreciation to my friends for their unwavering support and encouragement throughout my studies. And thanks to Tom McCoy for his companionship and for reviewing my English for this work.

Last but not least, I thank my family. My mom, Maria, my dad, Nelson, and my sister, Leticia, for their love and support, especially during hard times. Their unwavering support and encouragement have been a constant source of motivation.

Resumo

Os sensores CMOS monolíticos são particularmente atrativos para o rastreamento de partículas carregadas em experimentos de física de altas energias devido a características como baixo ruído, baixo consumo de potência, e baixo custo de fabricação. O projeto Tangerine tem como objetivo desenvolver e testar novos protótipos de detectores projetados em um novo processo de fabricação de complementary metal-oxide-semiconductor (CMOS) de 65 nm. Para melhorar ainda mais o desempenho desses sensores, esta dissertação investiga uma geometria alternativa de pixel - uma matriz de pixels hexagonais - que tem vários benefícios potenciais em relação às geometrias convencionais de pixel quadrado ou retangular.

Nesta dissertação, um design de sensor com pixel de formato hexagonal foi implementado em uma camada epitaxial de alta resistividade e, em seguida, simulado integrando um modelo detalhado de campo elétrico proveniente de uma simulação de elementos finitos usando o Technology Computer-Aided Design (TCAD) em uma simulação baseada em Monte Carlo com o framework Allpix². As simulações são realizadas para um sensor monolítico de pixel ativo (MAPS) em tecnologia CMOS de 65 nm, com duas disposições de pixel - padrão e n-gap - em um design de eletrodo de coleta pequeno.

O desempenho dessas disposições é comparado em termos de eficiência, tamanho de cluster e resolução. Uma breve comparação entre as geometrias de pixel quadrado e hexagonal também é conduzida. Os pixels hexagonais usados nas simulações têm um tamanho de 35 microns. Além disso, é feita uma comparação entre os formatos de pixel hexagonal e quadrado com a mesma área.

Os resultados indicam que a implementação de disposições em pixels hexagonais foi consistente com as simulações do sensor realizadas em pixels quadrados com o mesmo design e apresenta algumas melhorias em termos de eficiência e tamanho médio de cluster. Em conclusão, este trabalho destaca o potencial da matriz de pixel hexagonal para melhorar o desempenho dos MAPS em experimentos de física de altas energias e fornecem insights para o desenvolvimento futuro de sensores monolíticos de pixel ativo.

Palavras chave: silício, CMOS, sensores monolíticos de pixel ativo, MAPS, simulação eletrostática, simulação de Monte Carlo.

Abstract

Monolithic CMOS sensors are highly attractive devices for charged particle tracking in high-energy physics experiments due to the following characteristics: low noise, low power consumption, low material budget, and fabrication cost. Tangerine Project aims to develop and test new detector prototypes designed in a novel 65 nm complementary metal-oxide-semiconductor (CMOS) imaging process. To further improve the performance of these sensors, this thesis investigates an alternative pixel geometry - a hexagonal pixel grid - which has several potential benefits over conventional square or rectangular pixel geometries.

In this thesis, a sensor design with hexagonal pixels is implemented in a high-resistivity epitaxial layer and then simulated by integrating a detailed electric field model from finite element simulation using Technology Computer-Aided Design (TCAD) into a Monte Carlo based simulation with the Allpix² framework. The simulations are conducted for a monolithic active pixel sensor (MAPS) in a 65 nm CMOS technology, with two pixel layouts - standard and n-gap - in a small collection electrode design.

The performance of these layouts is compared in terms of efficiency, cluster size, and resolution. A brief comparison between square and hexagonal pixel geometries is also conducted. The hexagonal pixels used in the simulations have a size of 35 microns. Additionally, a comparison is made between the hexagonal and square pixels with the same area.

The investigations of this thesis highlight the potential of the hexagonal pixel grid for improving the performance of MAPS in high-energy physics experiments and provide insights for the development of future monolithic active pixel sensors.

Keywords: silicon, CMOS, monolithic active pixel sensors, MAPS, Electrostatic Simulation, Monte Carlo simulation.

List of Figures

2.1	The schematic illustrates the energy band arrangement in conductors, semi-conductors, and insulators.	17
2.2	Crystal lattice illustration for intrinsic silicon, and silicon doped with n-type and p-type.	19
2.3	Average energy loss by a muon crossing copper for different momentum ranges [18]. The dashed lines are the components of the different interactions while the solid line is the total stopping power.	21
3.1	A schematic illustration of a hybrid, with bump-bond interconnection, assembly is presented	27
3.2	Schematic representation of a monolithic CMOS sensor with large collection-electrode (left) and small collection-electrode (right).	27
3.3	Schematic illustration of the small collection electrode in standard process fabrication (one unit cell). The dashed lines illustrate the edges of the depleted regions, showing the partial depletion of the sensor [30]. Not in scale.	28
3.4	Schematic illustration of the small collection electrode for the fabrication in the blanket process (left) and the n-gap process (right), showing the full lateral depletion[30]. Not in scale.	29
3.5	Pitch definitions in hexagonal and square pixels. For regular square and hexagonal pixels $px = py$	30
3.6	2D hexagonal grid coordinates.	31
4.1	Process flow of simulation tools by Synopsys Sentaurus TCAD	33
4.2	Illustration of a cross-section (a) and top view (b) of a simulated pixel. Not in scale.	34
4.3	Two-dimensional cross-section of the pixel cell. The mesh structure is depicted as black lines. Further details of the results will be explained in section 5.1.	37
4.4	Simulation flow executed with Allpix ² , which includes the names of the configuration files used in this thesis. The detector geometry and model configurations are input files for the two steps of the simulation (ETA Calculation and ETA Correction), explained in the following subsections.	41
4.5	Typical simulation flow with Allpix ² , which includes the names of the modules used.	43
5.1	The 3D simulated structure for standard process simulation for pitch size of 35 μm . The collection electrode is located at the center of the structure.	52
5.2	Doping concentrations results from the electrostatic simulation for (a) standard and (b) n-gap layouts for pixel pitch 18 μm . The white lines indicate the boundary of the depleted volume, and the gray structures represent the corresponding terminals where voltages were applied via metal contacts.	52

5.3	Doping concentrations results from the electrostatic simulation for (a) standard and (b) n-gap layouts for pixel pitch $35 \mu\text{m}$	52
5.4	Electric field strength results from the electrostatic simulation for (a) standard and (b) n-gap layouts for pixel pitch $18 \mu\text{m}$. The white lines indicate the boundary of the depleted volume.	53
5.5	Electric field strength results from the electrostatic simulation for (a) standard and (b) n-gap layouts for pixel pitch $35 \mu\text{m}$	53
5.6	Lateral electric field strength for (a) standard and (b) n-gap layouts for pixel pitch $18 \mu\text{m}$. The white lines indicate the boundary of the depleted volume.	53
5.7	Lateral electric field strength for (a) standard and (b) n-gap layouts for pixel pitch $35 \mu\text{m}$. The white lines indicate the boundary of the depleted volume.	54
5.8	Geant4 visualization of the simulated detector (grey box). Ten 5 GeV single-electron events cross the sensor (red arrows). The visualization is obtained with the [VisualizationGeant4] module in Allpix ²	54
5.9	Line graphs for standard (a) and n-gap (b) layouts. The ionizing particle (with the initial position indicated by the black arrow) cross the sensor along the z-axis between two adjacent pixels (with collection electrodes indicated by red arrows).	55
5.10	In-pixel representation of the cluster size for simulation at the threshold of (a) 20e, (b) 40e, and (c) 140e for a pixel size of $35 \mu\text{m}$ for standard layout.	56
5.11	In-pixel representation of the cluster size for simulation at the threshold of (a) 20e, (b) 40e, and (c) 140e for a pixel size of $35 \mu\text{m}$ for n-gap layout.	57
5.12	Cluster size histogram for multiple thresholds for standard layout (a) and n-gap layout (b).	57
5.13	Mean cluster size as a function of the energy threshold for the pixel size of $35 \mu\text{m}$. Statistical errors in the simulation results are small due to a large number of simulated events (500,000 per configuration)	58
5.14	Mean cluster size as a function of the energy threshold for square and hexagonal pixel with approximately the same area, with pitch $14.5 \mu\text{m}$ [44] and $18 \mu\text{m}$, respectively.	59
5.15	In-pixel representation of the efficiency at the threshold of (a) 20e, (b) 40e, and (c) 140e for a pixel size of $35 \mu\text{m}$ for standard layout.	60
5.16	In-pixel representation of the efficiency at the threshold of (a) 20e, (b) 40e, and (c) 140e for a pixel size of $35 \mu\text{m}$ for n-gap layout.	60
5.17	Mean efficiency as a function of the energy threshold for the pixel size of $35 \mu\text{m}$	61
5.18	Mean efficiency as a function of the energy threshold for a square and a hexagonal pixel with approximately the same area, with pitch $14.5 \mu\text{m}$ [44] and $18 \mu\text{m}$, respectively.	61
5.19	Coordinates used to calculate the residuals in polar coordinates, where r_{track} is the MC position of the incoming particle, and r_{cluster} is the reconstructed cluster position in polar coordinates.	62
5.20	Residual histograms before and after <i>eta</i> correction for pixel pitch $35 \mu\text{m}$. Histograms acquired at threshold 60e.	63
5.21	Residual histograms before and after <i>eta</i> correction for pixel pitch $18 \mu\text{m}$. Histograms acquired at threshold 60e.	64
5.22	Spatial resolution as a function of the energy threshold for the pixel size of $35 \mu\text{m}$	64

5.23 Spatial resolution as a function of the energy threshold for square and hexagonal pixel with approximately the same area, with pitch $14.5 \mu m$ [44] and $18 \mu m$, respectively.	65
--	----

List of Tables

4.1	Overview of layer structure of pixel model, along with the corresponding materials that constitute each part. Some key size and voltage parameters that were used for the simulation are also presented.	35
-----	--	----

Abbreviations List

ASIC	Application-Specific Integrated Circuit
CMOS	Complementary Metal-Oxide-Semiconductor
CLIC	Compact Linear Collider
FCC	Future Circular Collider
HEP	High Energy Physics
ILC	International Linear Collider
LHC	Large Hadron Collider
MAPS	Monolithic Active Pixel Sensors
MC	Monte Carlo
MIP	Minimum Ionizing Particles
PAI	Photoabsorption Ionization Model
SDE	Sentaurus Structure Editor
SDEVICE	Sentaurus Device
Si	Silicon
SRH	Shockley-Read-Hall
SVISUAL	Sentaurus Visual
SWB	Sentaurus Workbench
TCAD	Technology Computer-Aided Design
TSVs	Through-silicon vias

Contents

Chapter 1 - Introduction	14
1.1 Thesis Outline	15
Chapter 2 - Fundamentals of Semiconductor Physics	16
2.1 Basics of Semiconductor Physics	16
2.1.1 Intrinsic and Extrinsic Semiconductors	18
2.1.2 p-n Junction	19
2.2 Principles of Radiation Interaction with Matter	20
2.3 Physical Models for Semiconductors	21
2.3.1 Drift	22
2.3.2 Diffusion	23
2.3.3 Charge Carrier Recombination	23
Chapter 3 - Silicon Pixel Detectors	25
3.1 Silicon Pixel Detector Types	25
3.1.1 Monolithic Active Pixel Sensors with Small Collection Electrode	27
3.2 Hexagonal Pixel Geometry	30
Chapter 4 - Detector Simulation	32
4.1 Electrostatic Simulations	33
4.1.1 Device Geometry	34
4.2 Physics Model	37
4.3 Monte Carlo Simulations	40
4.3.1 Allpix ² Simulation Flow	40
Chapter 5 - Simulation Results and Discussions	51
5.1 Electrostatic Simulations	51
5.2 Monte Carlo Simulations	54
5.2.1 Cluster Size	55
5.2.2 Detection Efficiency	59
5.2.3 Spatial Resolution	62
Chapter 6 - Conclusions	66
Bibliography	68
Appendices	74
Appendix A	74
Appendix B	76
Appendix C	79

Chapter 1

Introduction

Pixel detectors for precise particle tracking have improved significantly over the past two decades and can now be found in the vast majority of current physics experiments and research facilities. The main experiments at the Large Hadron Collider (LHC), such as ATLAS [1], CMS [2], ALICE [3], and LHCb [4], use hybrid pixel vertex detectors close to the interaction point.

The design of a pixel sensor, in particular, is tailored to a specific application. Therefore, researchers must select the most suitable technology for each detector subsystem depending on the key aspects of their experiment. For instance, many desirable features, such as low noise, high detection efficiency, high energy, and spatial resolution are challenging to combine in one detector. It is therefore up to the researcher to select which characteristics are the most pertinent to their experiment. At present, hybrid pixel detectors are the preferred choice for meeting these demands and are considered to be the state-of-the-art technology in instrumentation [5]. On the other hand, monolithic pixel detectors are also attractive due to their simple and compact design. By integrating the sensor and readout electronics into a single monolithic silicon substrate, these detectors exhibit reduced production cost, lower material budget, and reduced complexity in module assembly [6]. Monolithic detectors are becoming increasingly popular in applications where small pixel size and low power consumption are important factors [5, 7, 8].

Pixel sensors rely on the electrical and optical properties of semiconductors to detect and measure incoming particles. The behavior of these sensors is dependent on several fundamental physical processes such as charge generation, charge collection, and signal readout. It is therefore crucial to have a thorough understanding of the underlying physics of semiconductors in order to interpret the functional behavior of pixel sensors accurately. Furthermore, the

demands for higher precision and greater data acquisition rates are driving the development of new particle detectors. This is particularly important for next-generation colliders such as the Future Circular Collider (FCC) [9], Compact Linear Collider (CLIC) [10], and International Linear Collider (ILC) [11], which will push the limits of particle physics by colliding particles at even higher energies. In this context, the detector simulation plays a key role in the development of new particle detectors by allowing for the precise modeling of the conversion of energy deposition into a signal. This simulation capability enables researchers to test and optimize the performance of new detector designs before they are built, leading to improved performance and reduced costs. The accuracy of the simulation can then be verified through test beam experiments.

Multiple studies are being conducted as part of the Tangerine Project [6] to show the capability of 65 nm CMOS (Complementary Metal-Oxide-Semiconductor) imaging technology, which is a manufacturing technique employed to fabricate imaging detectors for applications such as in high-energy physics. All of the simulations being run offer insightful information on the sensors, expanding our understanding of this cutting-edge technology and enhancing the creation of new prototypes. One of the main objectives is to characterize new prototypes and compare them to sensor simulations.

The goal of this study is to contribute to the development and characterization of forthcoming detector prototypes by assessing and measuring the characteristics of CMOS imaging sensors using hexagonal pixels. With fewer nearby pixels, less charge sharing, and a higher single-pixel signal-to-noise ratio, the hexagonal pixel can offer improvements in resolution and detection efficiency. This research evaluates and quantifies these characteristics.

1.1 Thesis Outline

The thesis is divided into six chapters, starting with a review of the physical concepts and notions that were retrieved from the literature and applied to the project in Chapter 2. Chapter 3 provides an overview of silicon pixel sensors, highlighting the differences between hybrid and monolithic sensors and describing hexagonal pixels. Chapter 4 gives an overview of the methodology and algorithms used for electrostatic and MC simulations. Chapter 5 presents the results obtained from the simulations and discusses their outcomes. Finally, Chapter 6 concludes the work, offering suggestions for future research and implementation.

Chapter 2

Fundamentals of Semiconductor Physics

In High-Energy Physics (HEP) experiments, the tracking detectors play a crucial role in providing vital information about the position and timing of crossing particles. For this purpose, silicon (Si) is most commonly used for high-precision detectors and manufacturing electronics. This material has undergone extensive research and development, making it the dominant choice for the production of readout chips and other electronic components [12].

The fundamental principles of semiconductor physics are presented in this chapter to provide a theoretical foundation for the results shown in subsequent chapters. The focus is on models that are applicable to this thesis, such as particle detection mechanisms, semiconductor properties, and charge transport in silicon. These topics are necessary inputs for the simulations described in Chapter 4. A more detailed description of semiconductor physics can be found e.g in [12] and [13].

2.1 Basics of Semiconductor Physics

Conductivity or resistivity and energy bands are the criteria used to classify solids into conductors, semiconductors, or insulators. Figure 2.1 depicts the structure of the band gap for various materials, where E_F is the Fermi level (the maximum energy level that an electron may occupy at temperature 0 K). The movement of electrons in the conduction band, which represents the range of energy levels where electrons can freely move and contribute to electrical conduction, induces electrical conductivity. In conductors, the conduction band is always filled with electrons, allowing for higher conductivity. On the other hand, insulators have the largest band gap, therefore moving electrons into the conduction band requires a prohibitively

large amount of energy. In contrast, semiconductors possess a relatively small band gap that enables a significant fraction of the valence electrons, which occupy the lower energy levels in the valence band, to transition into the conduction band with sufficient energy.

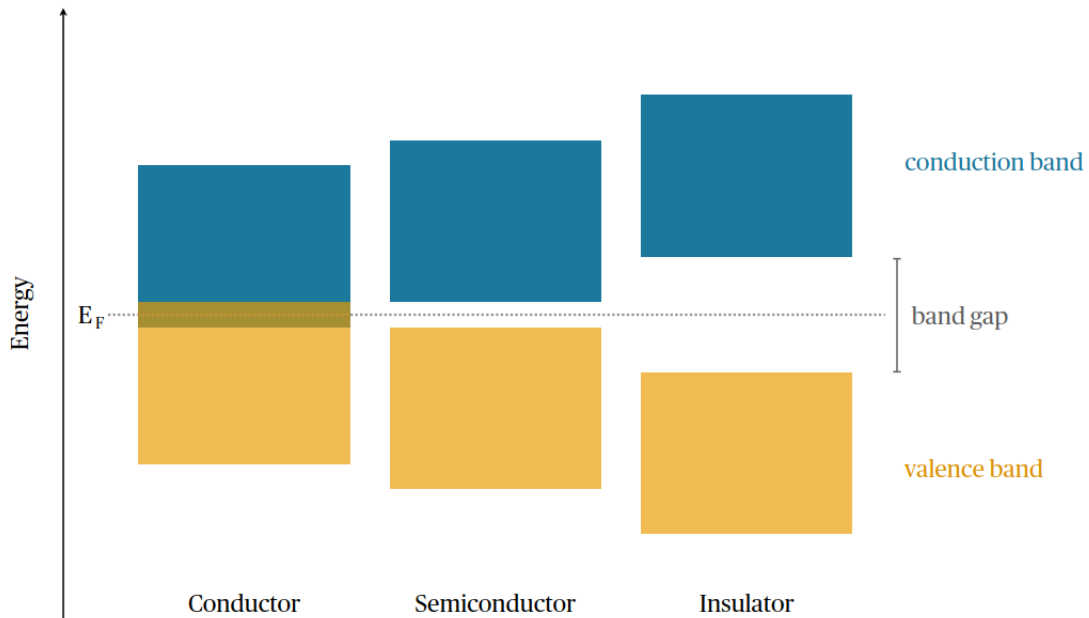


Figure 2.1: The schematic illustrates the energy band arrangement in conductors, semiconductors, and insulators.

The conductivity of semiconductors is highly temperature dependent. At lower temperatures, they behave as insulators, whereas at higher temperatures, they act as conductors. Conduction occurs at higher temperatures because the electrons around the semiconductor atoms may break free from their covalent link and travel freely across the lattice, which refers to the three-dimensional arrangement of atoms or ions in a crystal structure. The conductive property of semiconductors is the foundation for understanding how these materials may be used in electrical devices. The energy gap between the conduction and valence bands is dictated by the lattice constant of the material, which represents the characteristic distance between the atoms or ions in the crystal lattice. Therefore, the size of the band gap can be influenced by temperature and external pressure [14].

Semiconductors have been used in particle detectors since the early 1960s [12]. Compared to gaseous detectors, which require approximately 30 eV for gas ionization, silicon detectors provide a better energy resolution [15] because only 3.6 eV are required to generate electron-hole pairs with a band gap of 1.12 eV at room temperature. Furthermore, a good signal-to-noise ratio can be achieved even with a thin silicon wafer, allowing silicon to be used for

measurements of trajectories very close to the collision without an excessive material budget or increasing multiple scattering in the material.

2.1.1 Intrinsic and Extrinsic Semiconductors

Based on the purity of the material, there are two types of semiconductors: intrinsic and extrinsic.

Intrinsic semiconductors, characterized by minimal impurities, exhibit a disparity between the number of thermally generated electrons and holes [13]. In thermal equilibrium, the generation and recombination processes of electrons in the conduction band and holes in the valence band reach a balance, resulting in $n = p = n_i$, or

$$n \cdot p = n_i^2 = \text{const} \quad (2.1)$$

where n represents the concentration of electrons, and p represents the concentration of holes. This means that at equilibrium, the number of electrons in the conduction band is equal to the number of holes in the valence band, and both are equal to the intrinsic charge carrier density, n_i .

The intrinsic charge carrier density of silicon at 300 K is approximately 10^{10} cm^{-3} [12, 16]. However, when a MIP (Minimum Ionizing Particle) passes through a silicon layer with a thickness of $300 \mu\text{m}$, it generates approximately 3×10^4 electron-hole pairs [17]. Consequently, the resulting signal would be lost due to a large number of existing free charge carriers. Therefore, it becomes necessary to significantly reduce the number of free charge carriers. This can be achieved by using p- and n-type silicon in a reverse-biased pn-junction configuration. Such a configuration allows the depletion of free charge carriers from the volume of silicon, facilitating the detection of the desired signals.

In extrinsic semiconductors, the electrical properties of semiconductors can be modified by introducing impurities into the crystal lattice, which create additional energy levels between the conduction and valence bands. This process is called doping and depends on the type of materials introduced producing either n-type or p-type semiconductors. The n-type silicon has an excess of electrons in the conduction band, whereas the p-type silicon instead has holes (Fig. 2.2).

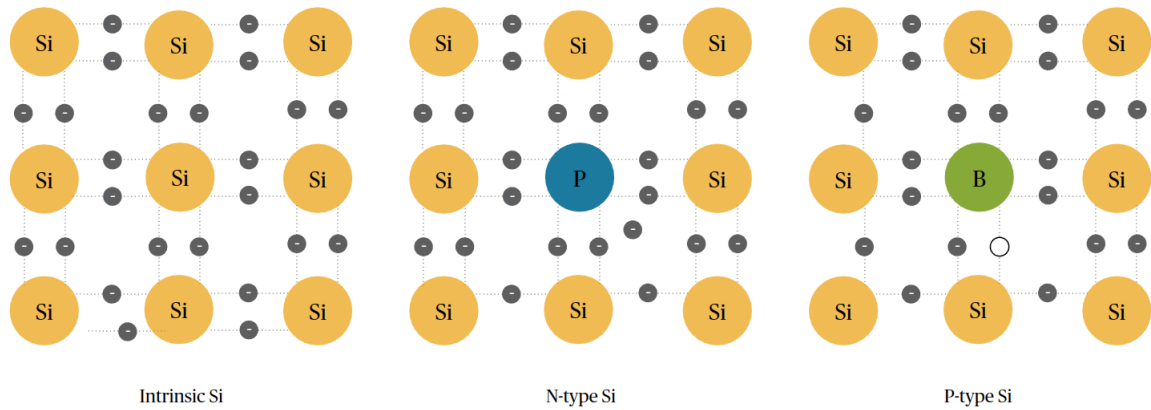


Figure 2.2: Crystal lattice illustration for intrinsic silicon, and silicon doped with n-type and p-type.

The n-type silicon is produced by adding impurities from group V of the periodic table, such as phosphorus or arsenic. In this case, donors add an excess of electrons (majority charge carrier) to the crystal. The p-type silicon is made with the introduction of group III elements, such as boron, where holes (the absence of electrons) are the majority of charge carriers. Group III impurities are called acceptors since they can capture electrons.

The doping concentration plays a key role in the design of silicon sensors, particularly in the establishment of pn-junctions that determine the electric field within the sensor. The electrical resistivity, which only depends on the density N of dopants and the mobility μ of the majority charge carriers, is a measure of the doping concentration and is given by:

$$\rho = (e \cdot N \cdot \mu)^{-1} \quad (2.2)$$

where e is the electron/hole charge.

The term *implant* refers to the localized implantation of dopants in a bulk substance. It frequently has high levels of doping concentrations, which are denoted by the symbols n^+ or p^+ .

2.1.2 p-n Junction

The p-n junction, formed by the juxtaposition of a p-type and an n-type region, is an essential electronic structure in semiconductor detectors. The junction creates an electric field that enables the collection of the charge generated by the radiation, moving them to the pixels and suppressing the leakage current, a source of noise in the sensor.

The interface region between the two doped materials loses free charge carriers due to the process of recombination between electrons and holes and is therefore known as the depletion region. The bound atoms at the depletion region are ionized, giving the n-doped portion of the junction a positive space charge and the p-doped material a negative space charge. As a result, there is an electrical field between the differently doped materials, which generates a current called the drift current, or I_{diff} . The diffusion current and drift are in thermal equilibrium in the absence of an external field. Applying an external reverse bias to the junction (i.e., a positive voltage on the p-side) will cause the depletion width to increase.

2.2 Principles of Radiation Interaction with Matter

The interaction mechanism of radiation with the detector material determines how effectively a radiation detector works. Analysis of the energy deposition from the radiation within the matter with which it is interacting is necessary to comprehend a specific response of a specific detector.

Charged particles lose energy when they penetrate a material by ionizing and exciting the atoms of the material. In semiconductors, this refers to the formation of electron-hole pairs, whereas in gaseous media it corresponds to the creation of free electrons and charged ions. Up until very high particle velocities, when radiation effects start to play a role, this is the primary method of energy loss for charged particles. The Bethe-Bloch formula reproduced in Equation 2.2, provides the mean energy loss along the trajectory's path for incoming heavy charged particles ($m \gg m_e$) [18].

$$-\left\langle \frac{dE}{dx} \right\rangle = 4\pi N_A r_e^e m_e c^2 \frac{Z}{A} \rho \frac{z^2}{\beta^2} \left[\frac{1}{2} \ln \frac{2m_e c^2 \beta^2 \gamma^2 T_{max}}{I^2} - \beta^2 - \frac{\delta(\beta\gamma)}{2} - \frac{C(\beta\gamma, I)}{Z} \right] [MeV g^{-1} cm^2] \quad (2.3)$$

Parameters are indicated in Appendix A.

Figure 2.3 shows the average of the deposited energy of a μ^2 when moving through copper, as a function of the relativistic factor, where v is the velocity in the observer's reference frame., $\beta = v/c$ and $\gamma = 1/\sqrt{1-\beta^2}$. The energy loss in a material is first-order independent of particle mass, therefore Equation 2.2 and the curve in Figure 2.3 can thus be viewed as universal. The range between 0.1 and 10^4 , which the Bethe-Bloch equation describes, is of particular interest.

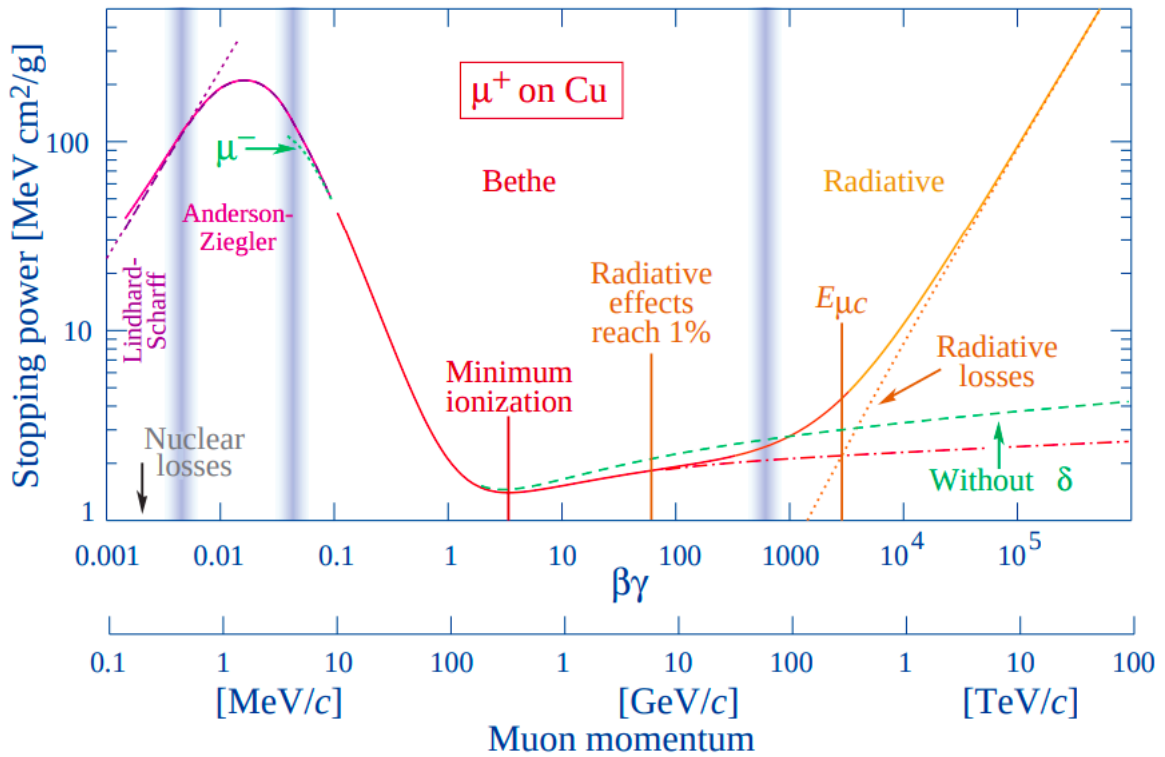


Figure 2.3: Average energy loss by a muon crossing copper for different momentum ranges [18]. The dashed lines are the components of the different interactions while the solid line is the total stopping power.

Equation 2.2 is typically parameterized in units of $\beta\gamma$ enabling the detection of distinctive energy loss ranges: at $\beta\gamma \ll 3$, particles are highly ionizing and deposit a large amount of energy in the material, while at $\beta\gamma > 3$, radiative processes lead to a shallow increase in energy loss. For particles with $\beta\gamma \sim 3$, a global minimum is reached and the energy loss is comparably low. Particles in this regime are referred to as MIPs.

MIPs are often used to quantify the detector response and is viewed as the worst-case situation for detectors as the given particle signal is the lowest. Thus, in order to detect MIPs, every detector should maintain its noise level significantly below this energy level.

2.3 Physical Models for Semiconductors

Section 2.1.2 described how the energy deposited by ionizing radiation is converted into electron-hole pairs, and also that the charge transport in semiconductors such as silicon involves two mechanisms: drift and diffusion.

2.3.1 Drift

In the presence of an electric field, a charged particle drifts the field lines. The traveling particle will scatter at random in the semiconductor lattice. The average velocity v of the object is then described by:

$$v_n = -\mu_n \cdot E \quad (2.4)$$

$$v_p = \mu_p \cdot E \quad (2.5)$$

with v_n for electrons and v_p for holes, each having its own mobility $\mu_{p/n}$.

In a strong electric field, the number of collisions in the lattice rises, compensating for the impact of increasing acceleration, resulting in drift velocity saturation. The charge carrier mobility is employed in the transport equations to account for these microscopic phenomena. It is influenced by a number of macroscopic factors, including temperature, doping level, and electric field.

The mobility can be influenced by a number of factors, including temperature, doping level, and electric field. Some available researched models only take temperature and doping concentration into consideration, resulting in less accurate but faster computation. Therefore, the choice of a proper model for a certain problem is crucial to the simulation.

The Jacoboni-Canali model [19][20] is the most often used parameterization of charge carrier mobility in silicon as a function of electric field E . Mobility models with saturation velocities, such as the Jacoboni-Canali model, can be extended with low-field models that take doping concentration into account, e.g the Masetti model [21]. The mobility is characterized as:

$$\mu(E, N) = \frac{\mu_m(N)}{(1 + (\mu_m(N) \cdot E/v_m)^\beta)^{1/\beta}} \quad (2.6)$$

where $\mu_m(N)$ is the Masetti mobility, and β and v_m are parameters defined for holes and electrons respectively.

2.3.2 Diffusion

The process of diffusion relies on the random walk of charge carriers within the material toward a region with a lower concentration of carriers. The behavior of the charge diffusion current can be described as:

$$J_{n,diff} = -D_n n = -\frac{kT}{q} \mu_n n \quad (2.7)$$

$$J_{p,diff} = -D_p p = -\frac{kT}{q} \mu_p p \quad (2.8)$$

where n and p are the gradients of electron and hole concentration respectively. D is the diffusion constant describing the random motion of charge carriers, written as:

$$D_{n,p} = \frac{\mu_{n,p} K_B T}{q} \quad (2.9)$$

with μ the mobility, K_B Boltzmann's constant and T the absolute temperature.

2.3.3 Charge Carrier Recombination

Generation and recombination take place when an electron moves from the valence band to the conduction band as a result of interactions with other electrons, holes, photons, or the vibrating crystal lattice, such as when ionizing radiation penetrates the semiconductor. To reach equilibrium, net recombination must take place, and this procedure is highly influenced by factors like temperature or doping level. Therefore, a recombination rate must be established for each semiconductor.

Shockley-Read-Hall Recombination

As the electron moves between bands, it can become trapped in a new energy state that has been generated within the band gap by a dopant or a defect in the crystal lattice; such energy states are known as traps. This process is known as Shockley-Read-Hall recombination (SRH) [22], also known as trap-assisted recombination. These energy levels are caused by lattice imperfections, or deep defect levels, which can increase when dopants are added.

If the recombination centers are near the center of the band gap, the lifetime of the charge carrier (τ_{SRH}) is provided by:

$$\tau_{SRH}(N_{d,e/h}) = \frac{\tau_{0,e/h}}{1 + N_{d,e/h}/N_{d0,e/h}} \quad (2.10)$$

where $N_{d,e/h}$ is the doping concentration, and $N_{d0,e/h}$ and $\tau_{0,e/h}$ are reference doping concentration and reference lifetime for electrons and holes, respectively.

Auger Recombination

In a three-particle process, the electron-hole couples recombine in band-to-band transitions, transferring any extra energy to another electron e (e-e-h process) or hole h (e-h-h process). The total recombination rate is then given by [23]:

$$R_A = C_n n^2 p + C_p n p^2 \quad (2.11)$$

where the e-e-h process is represented by the coefficient C_n , and the e-h-h process is represented by coefficient C_p . The minority charge carrier Auger lifetime in highly-doped silicon can be expressed as:

$$\tau_A = \frac{1}{C_A \cdot N_d^2} \quad (2.12)$$

where $C_A = C_n + C_p$ is the ambipolar Auger coefficient, taken as $C_A = 3.8 \times 10^{-31} \text{ cm}^6/\text{s}$ [24].

Combined Shockley-Read-Hall/Auger Recombination

The model combines [25] the charge carrier recombination from the Shockley-Read-Hall and the Auger models by inversely summing the separate lifetimes determined by the models as:

$$\begin{aligned} \tau^{-1} &= \tau_{SRH}^{-1} + \tau_A^{-1} && \text{minority charge carriers} \\ &= \tau_{SRH}^{-1} && \text{majority charge carriers} \end{aligned} \quad (2.13)$$

where $\tau_{SRH}(N)$ is the Shockley-Read-Hall and $\tau_A(N)$ the Auger lifetime .

Chapter 3

Silicon Pixel Detectors

A pixelated sensor is a system that incorporates a highly segmented periodic two-dimensional array of collecting diodes with biased junction regions. These charge-collecting electrodes are divided in two directions to achieve the required position resolution for tracking.

Silicon is widely used in detectors due to its extensive research and popularity as a semiconductor material in various fields of technology production. It possesses well-known electrical characteristics, is accessible in vast quantities at a reasonable cost, and has well-developed manufacturing techniques due to advances in the electronics industry. This has led to the development of highly advanced fabrication processes that are capable of producing high-quality and reliable silicon-based detectors [26] with high accuracy, stability, and long lifetimes. Silicon pixel detectors have been used in particle physics experiments since the early 1990s, with small-scale devices. Subsequently, sensors with millions of pixels were developed for LHC investigations [5].

3.1 Silicon Pixel Detector Types

Different silicon pixel detector types have previously been developed, each with specific benefits and limitations, as a result of the extensive implementations in HEP and the consequent diversified needs. The two primary categories of detectors are monolithic and hybrid detectors, both of which use silicon pixel technology.

- **Hybrid Pixel Detectors:** the pixel sensor and readout electronics are separate entities, which are connected through various methods such as bump bonding or through-silicon vias (TSVs). It is currently the preferred solution, particularly for applications

in high-rate and high-radiation conditions, such as at the LHC. The schematics of the hybrid sensor technology are shown in Figure 3.1.

Depending on the application, hybrid pixel detectors can be either energy integrating or photon-counting detectors. The detecting substrate is entirely depleted and can be composed of semiconductors other than silicon since it is independent of the readout electronics. Examples of such materials are CdTe, Ge, GaAs, CdZnTe, and other compounds depending on the application [27].

The ability to independently optimize the sensor and ASIC readout is a big advantage of the hybrid technology. However, the interconnection between the electronics and the sensor poses the primary challenge because it may increase the amount of material used, increase the cost of fabrication, and restrict the size of the pixels.

- **Monolithic Active Pixel Sensors (MAPS):** The readout electronics are built within the detecting volume. As a result, there is no need for connections between the components, which reduces the amount of sensor material. Monolithic sensors are typically created using commercially available CMOS fabrication techniques, with minor adjustments to make them suitable for HEP applications. Two main pixel designs were developed with different strategies: large collection electrodes and small collection electrodes.

- **Large collection electrode:** The electronic components of the sensor are separated from the rest of the device within the electrode, as shown in Figure 3.2a. This isolation allows for the use of a high bias voltage, creating a large depleted area and a uniform electric field. The design of the large collection electrode offers strong charge collection capabilities throughout the entire pixel region. The short average drift path to the collection electrode is shorter due to a fully depleted sensor area, which enhances radiation tolerance and decreases the likelihood of trapping.

Due to the need to fit the electronics, the size of the collection electrode may be affected, resulting in a high total capacitance at the preamplifier, which can limit the attainable signal-to-noise ratio.

- **Small collection electrode:** In this design, the readout electronics are positioned on isolated well structures, separate from the collection electrode, as shown in Figure 3.2b. Because of this, the electrode's size may be reduced, which is favorable for

a low sensor capacitance. However, the non-uniform depletion of the epitaxial layer in the sensor leads to a constraint on the charge collection time due to diffusion [28].

The intensity of the lateral electric field in the corner region can be enhanced by introducing a lateral gradient in the doping profile for faster charge collection by drift, reducing charge sharing. The strength of the lateral electric field in the pixel corner can be improved by inserting a lateral gradient in the doping profile for faster charge collection [29] (See subsection 3.1.1).

In this thesis, MAPS with small collection electrodes are being investigated. More details are provided in the following sections.

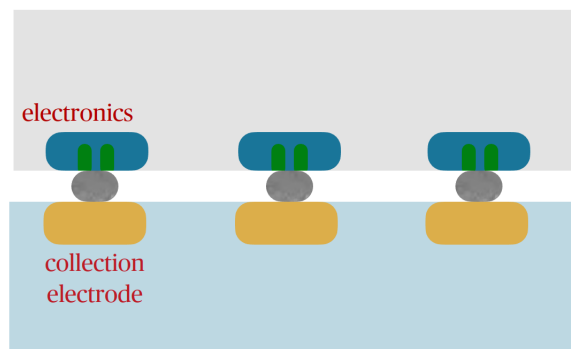


Figure 3.1: A schematic illustration of a hybrid, with bump-bond interconnection, assembly is presented

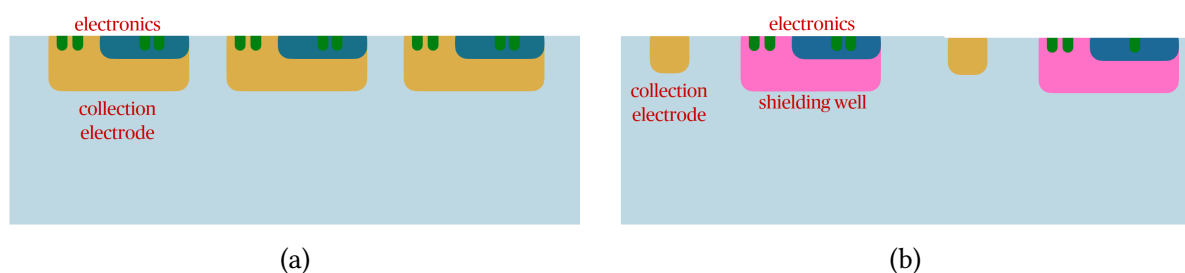


Figure 3.2: Schematic representation of a monolithic CMOS sensor with large collection-electrode (left) and small collection-electrode (right).

3.1.1 Monolithic Active Pixel Sensors with Small Collection Electrode

As depicted in Figure 3.2b, the readout electronics in the small collection-electrode design are implemented within separate well structures, isolated from the collection electrode. The simulated structures comprise a combination of p-type substrate with p-type shielding wells and an n-type collection electrode.

The foundation of the CMOS device is a silicon substrate with low resistivity. And the structures are described as follows:

- **Substrate:** The substrate serves as the base material on which the MAPS is fabricated. It is typically made of silicon and provides mechanical support for the sensor.
- **Epitaxial Layer:** The epitaxial layer, also known as the epi-layer, is a layer of semiconductor material grown on top of the substrate. It has a controlled thickness and doping profile. The epitaxial layer provides the foundation for forming the n and p wells and supports the formation of CMOS transistors.

For the purpose of this thesis, a $10\ \mu\text{m}$ thick thin epitaxial layer of lightly p-doped silicon was simulated on top of the substrate, resulting in a $50\ \mu\text{m}$ thick total sensor. Figure 3.3 displays the MAPS's detailed schematic with a small collection electrode.

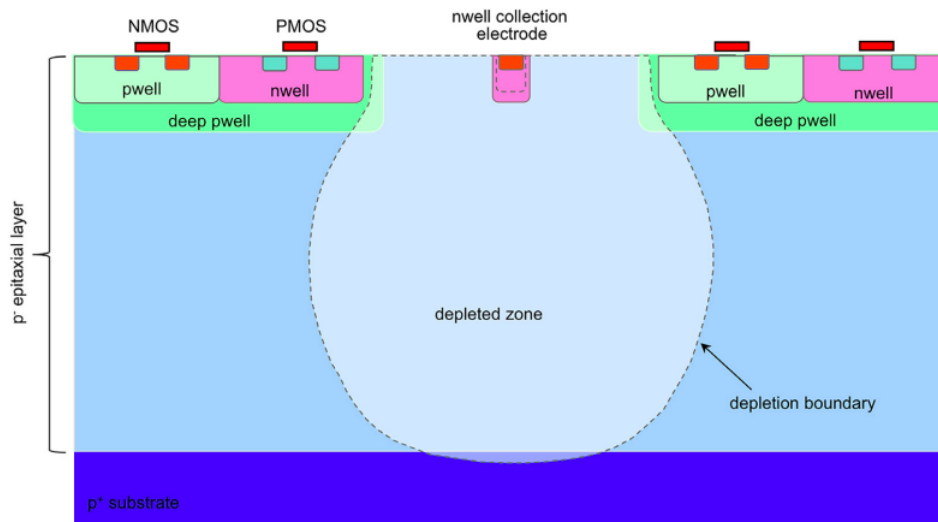


Figure 3.3: Schematic illustration of the small collection electrode in standard process fabrication (one unit cell). The dashed lines illustrate the edges of the depleted regions, showing the partial depletion of the sensor [30]. Not in scale.

- **n-wells:** The n-wells are regions within the epitaxial layer that are doped with n-type impurities. These wells are formed to create a collection electrode. When biased, the n wells generate an electric field that attracts electrons captured as signals during the detection process.
- **p-wells:** The p-wells are regions within the epitaxial layer that are heavily doped with p-type impurities. These wells are formed to create a collection electrode and house the CMOS transistors responsible for signal processing.

In order to apply bias voltages and extract signals from a sensor, an ohmic metal contact is placed adjacent to a highly-doped region in the silicon. In the presented sensors, contacts are made to the n-well (collection electrode), the p-well, and the sensor substrate. See subsection 4.1.1 for more details on voltage values and placements.

Pixel flavors

Electric fields are mostly absent from the silicon substrate and epitaxial layer, so any charge deposited there will diffuse at random paths to the collection electrode. The fabrication process can be modified to achieve full lateral depletion of the sensor volume by inserting a lateral gradient in the doping profile. Therefore, the investigated small-collection electrode sensor processes can be fabricated in different pixel flavors, such as standard, n-blanket, or n-gap.

The first flavor is the standard, as shown in Figure 3.3. The second variant, known as n-blanket and shown in Figure 3.4a, involves the addition of a continuous low-dose deep n-implant beneath the p-wells. This leads to complete lateral depletion in the epitaxial layer. In the third modification, the deep n-implant is placed away from the pixel edges to create a lateral doping gradient beneath the p-wells. This amplifies the lateral electric field, resulting in accelerated propagation of charge carriers towards the collection electrode. This modified configuration is referred to as n-gap, as depicted in Figure 3.4b.

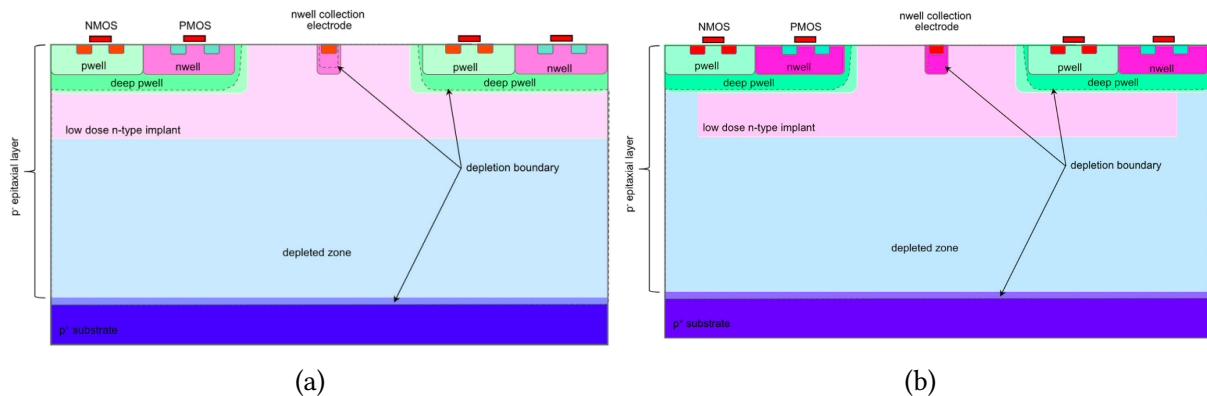


Figure 3.4: Schematic illustration of the small collection electrode for the fabrication in the blanket process (left) and the n-gap process (right), showing the full lateral depletion[30]. Not in scale.

Other process modifications can be produced for fast-timing applications that require sub-nanosecond resolution [28] but are not investigated in this thesis.

3.2 Hexagonal Pixel Geometry

In MAPS with small collection electrodes, the process of charge sharing occurs due to the combined effects of charge drift and diffusion as the generated charges from a particle move toward the collection electrodes. Various factors, including the pixel shape, can influence the extent of charge sharing and ultimately impact the performance of the sensor. Square and rectangular pixels are commonly used in fabrication due to their ease of manufacturing and well-defined charge-sharing patterns. These pixel shapes are straightforward to fabricate and provide a simple and well-understood charge-sharing pattern.

An alternate pixel sensor geometry to the rectangular/square pixel sensor geometry is a hexagonal pixel grid, which can offer a number of potential advantages, including higher efficiency and timing resolution. This pixel geometry is the focus of this thesis.

An alternative pixel sensor geometry that is of particular interest is the hexagonal pixel grid. This pixel geometry offers several potential advantages, such as high efficiency and improved timing resolution. The focus of this thesis is to investigate and analyze the characteristics and performance of the hexagonal pixel grid to gain a comprehensive understanding of its aspects.

Typically, the pitch of a pixel is determined by adding the pixel size and the spacing between neighboring pixels. However, for simplicity, it is typically regarded as the side length of the pixel in both the x and y directions in square pixels. In the context of this work, the pitch of a hexagonal pixel specifically refers to the distance between two opposing edges, as illustrated in Figure 3.5.

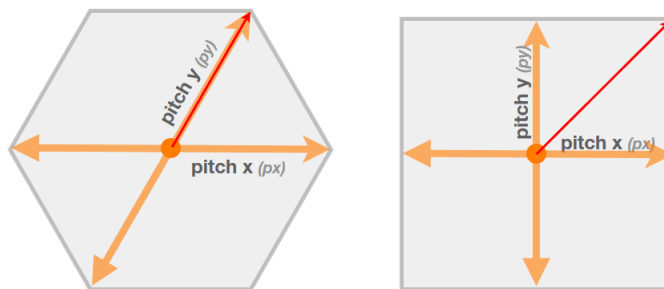


Figure 3.5: Pitch definitions in hexagonal and square pixels. For regular square and hexagonal pixels $px = py$

The hexagons investigated are regular, which means they represent a closed shape polygon with six equal sides and six equal angles. As a result, the pitch in both the x-direction (px) and y-direction (py) of the hexagon have the same length (see Figure 3.6).

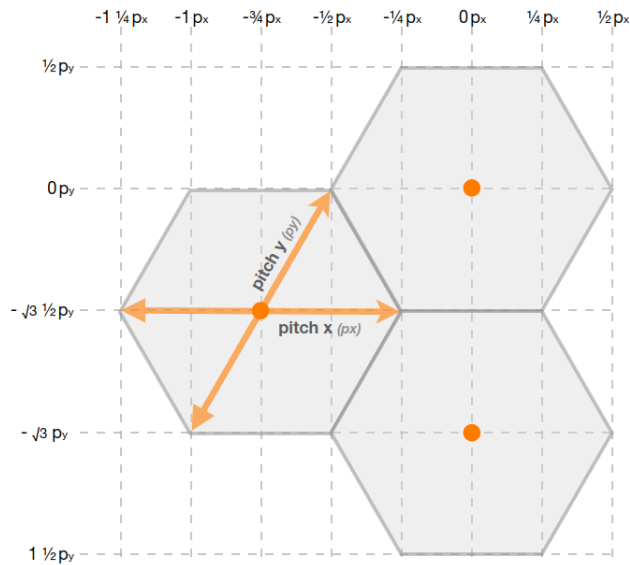


Figure 3.6: 2D hexagonal grid coordinates.

The comparison between hexagonal pixels and square pixels is particularly interesting when they have the same area. This is because the amount of electronics inside the p-well is a relevant factor to consider when comparing these two pixel shapes in MAPS. With hexagonal pixels, it is possible to achieve smaller pitch sizes while maintaining the same amount of electronics. This allows for a direct evaluation of the impact of pixel shape on various factors, including charge sharing, spatial resolution, and efficiency, while keeping the area constant. To establish a meaningful comparison between hexagonal and square pixels with the same area, we can derive the following relationship based on the definitions shown in Figure 3.5:

$$Pitch_{square} = \left(\sqrt{\frac{3\sqrt{3}}{2}} \right) \cdot \frac{Pitch_{hexagon}}{2} \quad (3.1)$$

In particular, simulated hexagonal pixels in honeycomb matrices are intriguing for many reasons. For instance, by limiting the maximum distance of the pixel boundary from the center while keeping the same area, hexagonal pixel shapes avoid complex electric field regions in the pixel corners. The maximum distance in the square grid between the pixel corner and the collection electrode (red line in Figure 3.5) drops approximately 12% for the same pixel area on a hexagonal grid [28].

The hexagonal design also contributes by reducing charge sharing at the pixel corners from four to just three pixels. As charge sharing is decreased, the signal in the seed pixel increases as charge sharing is reduced.

Chapter 4

Detector Simulation

In the semiconductor industry and academic research for particle detector development, simulation is used to study the fundamental physics of particle interactions with matter, the charge collection and transport processes in detectors, and the behavior of new and emerging devices under various conditions. In particular, small collection-electrode monolithic silicon sensors have complicated non-uniform field compositions that require the use of simulations to fully understand and optimize its performance.

The electrostatic field simulations provide information about the electrical characteristics of the device, such as the distribution of electric charges and doping concentration profile, taking into account the physical and electrical properties of the materials used in the device. MC simulations, on the other hand, model the behavior of charged particles, as they traverse the sensor, accounting for the interactions between the particles and the materials in the device. This chapter describes a method for combining MC and electrostatic field simulations.

[SYNOPTIS' Technology Computer-Aided Design \(TCAD\)](#) tool (Version R-2020.09-SP1) was selected as a tool for electrostatic simulations and computed electric fields were integrated with Geant4 simulations of particle interactions with matter via the Allpix² framework. As a result, we can examine the behavior of MAPS detectors, and analyze and compare predicted performance to known or expected behaviors. To have the full picture of the sensor performance, different sensor layouts have been simulated.

The schematic of the simulation framework is shown in Figure 4.1, starting from Sentaurus Workbench (SWB), which determines the changing parameters managing the simulation. The creation of a device structure is simulated by SDE, and then SDEVICE is used to simulate the electrical properties of the device. Finally, SVISUAL is used to visualize the result from the simulation in 2D and 3D.

4.1.1 Device Geometry

In section 3.2, we introduced pixel geometry that was implemented in SDE. A three-dimensional (3D) model has been created due to the constraints of a two-dimensional projection, which may fail to represent certain effects happening at the corners of the pixels.

Figure 4.2 displays the simulated structure of a pixel cell, with the z direction following the sensor depth, the x direction being parallel to the hexagon's apothem, and the y direction following py , as depicted in Figure 3.6.

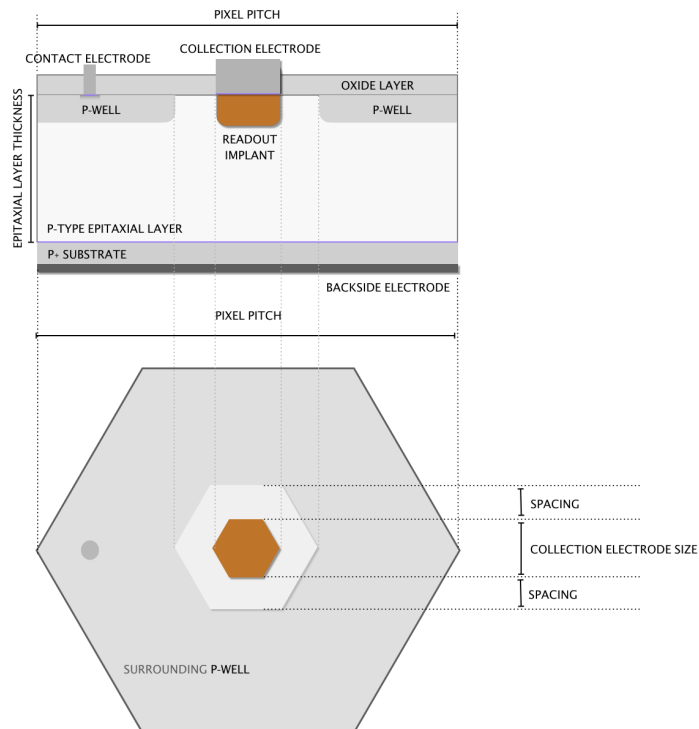


Figure 4.2: Illustration of a cross-section (a) and top view (b) of a simulated pixel. Not in scale.

In TCAD simulations, the number of simulated pixels depends on the size and complexity of the analyzed device or structure. Conversely, in Allpix² Monte Carlo simulations, the number of simulated pixels is determined by the size and granularity of the modeled detector (refer to section 5.2). Therefore, due to the significant computational time and memory

requirements associated with electrostatic simulations for larger and more complex pixels, it is convenient to simulate only a single-pixel structure on TCAD. The subsequent steps of the detector simulation in Allpix² assume symmetry when constructing a pixel matrix, thereby reducing the computational effort.

Additionally, the substrate, which resides beneath the epitaxial layer, is typically excluded from TCAD simulations since its impact on 3D TCAD studies is minimal due to the absence of an electric field in that region. Instead, the substrate is included in Monte Carlo simulations to optimize computational resources. Table 4.1 provides a comprehensive list of layer structures for the sensor simulated with TCAD, along with the corresponding materials that constitute each component.

Table 4.1: Overview of layer structure of pixel model, along with the corresponding materials that constitute each part. Some key size and voltage parameters that were used for the simulation are also presented.

Layer Description	Material	Observations
oxide	SiO ²	
collection electrode	aluminum	applied voltage 1.2 V
contact electrode	aluminum	applied voltage -1.2 V
backside electrode	aluminum	applied voltage -1.2 V
p-epi layer	silicon - boron doped	thickness 10 μm
readout implant	silicon - phosphorus doped	width 0.8 for pixel pitch 35 μm
p-well	silicon - boron doped	spacing from readout implant approx 0.6 μm

Doping Concentrations

In addition to specifying the geometry of a structure, doping concentrations have to be defined for different parts of the structure. The accuracy of TCAD simulations heavily relies on the precision of doping profile models, and the absence or uncertainty of this information can impact the reliability of the simulation outcomes. However, the detailed doping values are considered confidential by the foundry, and no confidential information regarding the substrate doping concentration levels of the high-resistivity wafers was accessible in this study.

As a result, generic doping profiles have been used assuming gaussian distribution and consisting of approximate doping concentrations for the different regions. The approximate doping levels used are $1 \times 10^{18} \text{ cm}^{-3}$ for the substrate, less than $1 \times 10^{13} \text{ cm}^{-3}$ for the epitaxial layer [32].

Setting and optimizing a few boundary conditions can also help improve the simulation accuracy. One crucial aspect to consider is the prevention of nonphysical effects caused by abrupt changes in doping concentration and the resulting electric field. To achieve this, it is necessary to appropriately diffuse the doping profiles at the interfaces between different doping structures, such as n- and p-wells and the epitaxial layer/substrate. This diffusion ensures a smooth transition in the doping profile and can be defined through Gaussian or the complementary error function.

For instance, the p-substrate is doped uniformly with boron atoms, and the epitaxial layer displays a similar uniform doping profile but with a reduced doping concentration. Therefore, the concentration diffusion technique can be employed in the transition regions located at the bottom of the epitaxial layer where it interfaces with the substrate, as well as at the n- and p-well edges.

Mesh Generation

In finite-element simulations, the simulation solution of the Poisson equation is computed through mesh element corners. Therefore, the granularity of the mesh is crucial for the accuracy of the simulation because the solutions become inaccurate or there is no convergence if the mesh is too coarse.

However, it is difficult to choose the optimal mesh sizes for solving the problem while ensuring convergence and, at the same time, running a fast simulation. To address this issue, a strategy is employed where high grid density is applied in regions characterized by significant gradients in geometric and physical quantities of interest. These regions typically include junctions and doping transitions, where precise modeling is important. In Figure 4.3, a cross-section of a simulated mesh is depicted, represented by black lines. In 2D simulations, the mesh comprises triangles, while in 3D simulations, it consists of tetrahedra.

The value within each electric field vector component for every mesh node and the vertex coordinates of each node may later be exported from the TCAD DF-ISE data. This will then be entered into the MC simulations that are explained in section 4.3.

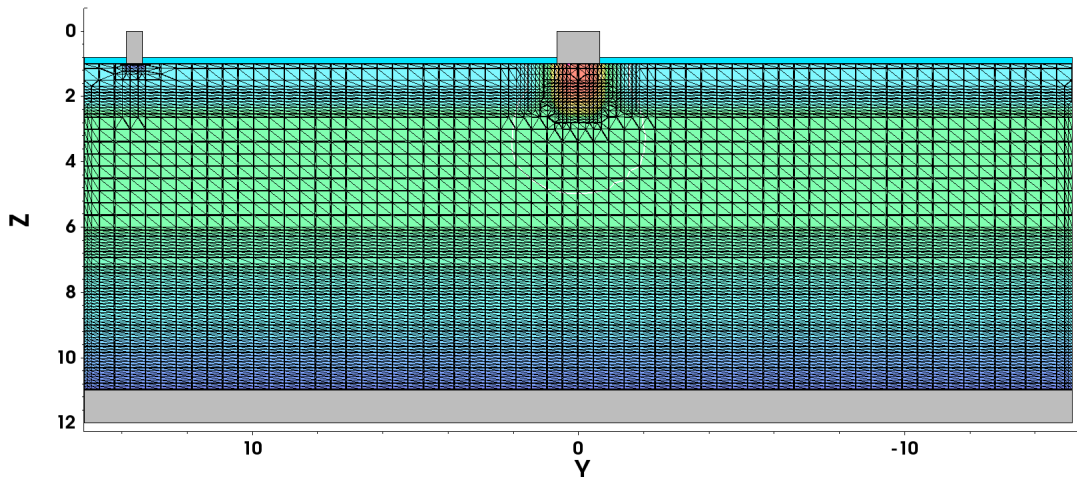


Figure 4.3: Two-dimensional cross-section of the pixel cell. The mesh structure is depicted as black lines. Further details of the results will be explained in section 5.1.

4.2 Physics Model

TCAD solvers address three key problems: calculating the electrostatic potential using Poisson's equation, determining the electron and hole concentrations through the electron and hole continuity equations, and computing the electrostatic potential. The electrostatic potential translates to the voltage on physical contacts, while the net charge flux translates into electric current. Terminal currents, voltages, and charges are computed based on a set of physical device equations that describe the distribution of carriers and conduction mechanisms (see Section 2.3).

Quasi-stationary simulations were performed using SDEVICE. The applied voltage is gradually increased until it reaches a specified value, and the resulting electric field is measured [33]. At steady-state, the partial derivative of each property with respect to time is zero.

To solve the equations related to mobility, generation, and recombination rates, TCAD software provides a wide range of models. The specific configurations for the physical models required to perform electric field simulations are described below, and the corresponding code snippet is presented in Listing 4.1.

- **Temperature:** Sdevice offers computation of three temperatures: lattice temperature, electron temperature, and hole temperature. The lattice temperature accounts for self-heating effects of the device.

As an initial estimate, the electron and hole temperatures are set to the lattice temperature. For carriers whose temperatures are not explicitly solved, they are assumed to have the lattice temperature throughout the simulation.

- **Fermi Statistics:** The Fermi statistics were employed to calculate the electron and hole densities [33].

In the active regions of a silicon device, such as in the presence of applied bias or high doping levels, the carrier densities can reach high values. Under these conditions, the importance of Fermi statistics becomes particularly relevant.

The density of charge carriers is described by:

$$n = \gamma_n N_C \exp\left(\frac{E_{F,n} - E_C}{kT}\right) \quad (4.1)$$

$$p = \gamma_p N_V \exp\left(\frac{E_V - E_{F,p}}{kT}\right) \quad (4.2)$$

Where γ_n and γ_p are the functions of the carrier quasi Fermi energy η_n and η_p , given as:

$$\gamma_n = \frac{n}{N_C} \exp(-\eta_n) \quad (4.3)$$

$$\gamma_p = \frac{p}{N_V} \exp(-\eta_p) \quad (4.4)$$

$$\eta_n = \frac{E_{F,n} - E_C}{kT} \quad (4.5)$$

$$\eta_p = \frac{E_V - E_{F,p}}{kT} \quad (4.6)$$

- **Carrier Mobility:** Masetti model [21] for doping-dependent mobility referenced as `DopingDependence` at the code below, and Canali model for high-field saturation referred as `eHighFieldSaturation` or `hHighFieldSaturation`.
- **Recombination model:** Shockley-Read-Hall Recombination (SRH) model enabled as `Recombination` (see subsection 2.3.3)

- **Band Structure Model:** Band gap narrowing model Slotboom model [34] (keyword `Slotboom`) for a highly doped substrate. In Sentaurus Device, the approach to modeling bandgap narrowing takes the following form:

$$E_{bgn} = \Delta E_g^0 + \Delta E_g^{Fermi} \quad (4.7)$$

where ΔE_g^0 is determined by the specific bandgap narrowing model used, and ΔE_g^{Fermi} is an adjustment to take carrier statistics into account [33].

Bandgap narrowing for the Slotboom model measures the narrowing in relation to the total amount of doping [35]. This empirical method combines a number of physical phenomena, including electron-electron interactions, carrier-impurity interactions, random potential fluctuations, and electron-hole interactions, into a single energy narrowing parameter. As a result, the calculated band gap narrowing remains consistent in both neutral and depleted regions of the device. The following equation is used by the Slotboom model to calculate the band gap narrowing:

$$\Delta E_g^0 = E_{ref} \left[\ln \left(\frac{N_{tot}}{N_{ref}} \right) + \sqrt{\ln \left(\frac{N_{tot}}{N_{ref}} \right)^2 + 0.5} \right] \quad (4.8)$$

where E_{ref} and N_{ref} are material properties, available in Sentaurus Device.

```

1 Physics
2 {
3     Fermi
4     Temperature = 293
5     Mobility(
6         DopingDependence
7         eHighFieldSaturation
8         hHighFieldSaturation
9     )
10    Recombination(
11        SRH(
12            DopingDependence
13            TempDependence
14        )
15        eAvalanche
16        hAvalanche
17    )
18    EffectiveIntrinsicDensity (BandGapNarrowing(Slotboom))
19 }
```

Listing 4.1: Physics models definitions in SDEVICE configuration file.

4.3 Monte Carlo Simulations

Monte Carlo (MC) simulations are designed to computationally solve problems by executing stochastic simulations of a system. Using the appropriate algorithms and adequate random distribution sampling, MC simulations enable replicating the behavior of physical systems and processes.

In the context of particle detection, simulations involving sensitive components can typically be divided into three stages. First, the interaction between the particle and the sensor material is simulated using external event generators, as described in section 2.3. In the second stage, the trajectories of primary particles are tracked as they pass through the structures of the detector and interact with them. Finally, in the third stage, the particle hit information in the pixel is processed to estimate the resulting signals [36].

[Allpix²](#) (read: Allpix Squared) is an open-source software framework written for the complete end-to-end modeling simulation of semiconductor pixel detectors [37]. Alongside Geant4 and ROOT, Allpix² offers a wide range of capabilities, enabling researchers to investigate various aspects such as charge propagation, energy deposition, signal transmission, and digitization within a sensor.

For the purposes of this thesis, a modified version of Allpix² has been developed to execute simulations involving hexagonal pixels. This modified version incorporates specific enhancements and optimizations to better analyze and understand the behavior of hexagonal pixel detectors.

4.3.1 Allpix² Simulation Flow

The simulation process in Allpix² was divided into two steps and involved the use of four configuration files: the *detector model configuration*, the *detector geometry configuration*, and two *simulation configuration* files. Figure 4.4 presents a flowchart that provides an overview of the simulation workflow. In the following subsections, we will discuss each step of the simulation chain and provide examples of the corresponding configuration files needed to execute the simulation routine [25].

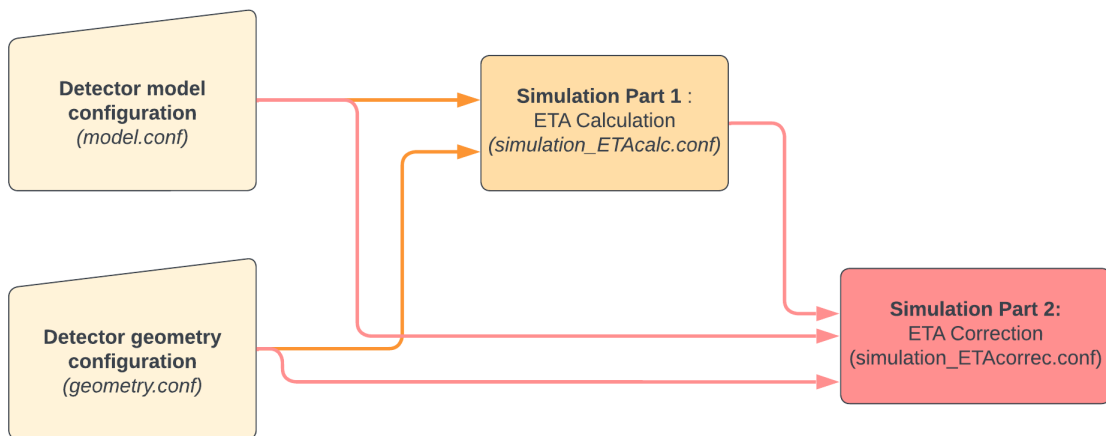


Figure 4.4: Simulation flow executed with Allpix², which includes the names of the configuration files used in this thesis. The detector geometry and model configurations are input files for the two steps of the simulation (ETA Calculation and ETA Correction), explained in the following subsections.

Detector model configuration

The detector model configuration describes the type of detector simulated, for example, a typical hybrid detector or monolithic pixel detector. The code piece of the configuration file is presented on Listing 4.2.

type: selects a monolithic pixel detector;

geometry: selects the geometry of the pixel (square or hexagonal);

number_of_pixels: the number of pixels in the detector in x and y directions;

pixel_size: pitch of the pixel in x and y directions;

pixel_type: selects the orientation of the pixel in x and y directions;

implant_size: readout implant size in x and y directions;

sensor_thickness: the thickness of the sensor in z direction (substrate+epitaxial layer);

sensor_excess_*: outside of the active pixel matrix, additional material is added to the pixel matrix on the top, bottom, left, and right orientations of the sensor. * should be substituted with top, bottom, left or right.

Detector geometry configuration

The geometry configuration defines the geometry of the simulated setup. The code piece of the configuration file is presented on Listing 4.3. The beginning of each section includes a title

```

1 type = "monolithic"
2 geometry = "hexagonal"
3 pixel_type = "hexagon_flat"
4
5 number_of_pixels = 100 100
6 pixel_size = 35um 35um
7 implant_size = 1.5um 1.5um
8
9 sensor_thickness = 50um
10 sensor_excess_top = 200um
11 sensor_excess_bottom = 200um
12 sensor_excess_left = 200um
13 sensor_excess_right = 200um

```

Listing 4.2: model.conf

that indicates the identification name of the detector. Every detector is required to contain all of the following parameters:

type: A text string is used to denote the type of the detector model, which refers to the configuration file of the model (*model.conf*).

position: 3D position in the global coordinate system x, y, z;

orientation: 3D rotation angles, specified as x-y-z extrinsic Euler angles.

```

1 [detector]
2 type = "model"
3 position = 0um 0um 0um
4 orientation = 0deg 0deg 0deg

```

Listing 4.3: geometry.conf

Simulation configuration part 1: eta Calculation

In detector simulations, conventional clustering methods typically assume linear charge sharing within the sensor and employ calculations based on arithmetic mean or charge-weighted center-of-gravity. For example, the center-of-gravity algorithm assumes that charge is shared linearly proportional to the distance between the electrodes. However, in scenarios involving bulk modifications like the n-gap layout and non-homogeneous electric fields, charges tend to be deflected towards the collection electrode, resulting in nonuniform charge sharing among neighboring pixels. To address this nonuniformity and accurately estimate the collected charge, the concept of the η -distribution (eta-distribution) is introduced. The eta-distribution provides a means to account for the nonuniform charge sharing and obtain more precise measurements of the collected charge.

To calculate the eta-distribution, the ratio $\frac{Q_{pixel}}{Q_{cluster}}$ is computed, where Q_{pixel} represents the charge on the reference pixel normalized to the cluster charge. The Allpix² module called

[EtaCalculation] performs a polynomial fit to determine the appropriate parameters for the non-linear charge sharing. It calculates the distributions for two-pixel clusters by comparing the track position and the calculated cluster center position. The recorded profiles are then fitted, and the resulting fits can be utilized in subsequent simulation steps.

The calculations of the distributions are performed for two-pixel clusters of any detector in the analysis by comparing the in-pixel track position and the calculated cluster center position. However, for hexagonal pixels, the transformation from the x and y axes to the polar coordinates ϕ and R is not straightforward. Since a hexagon can be approximated as a circle, the calculation is carried out in the x and y coordinates, but the data is treated in terms of polar coordinates ϕ and R.

Figure 4.5 illustrates a schematic of the simulation workflow employed in the MC simulations. In the subsequent paragraphs, we will introduce the models utilized in the simulations, along with their corresponding parameters.

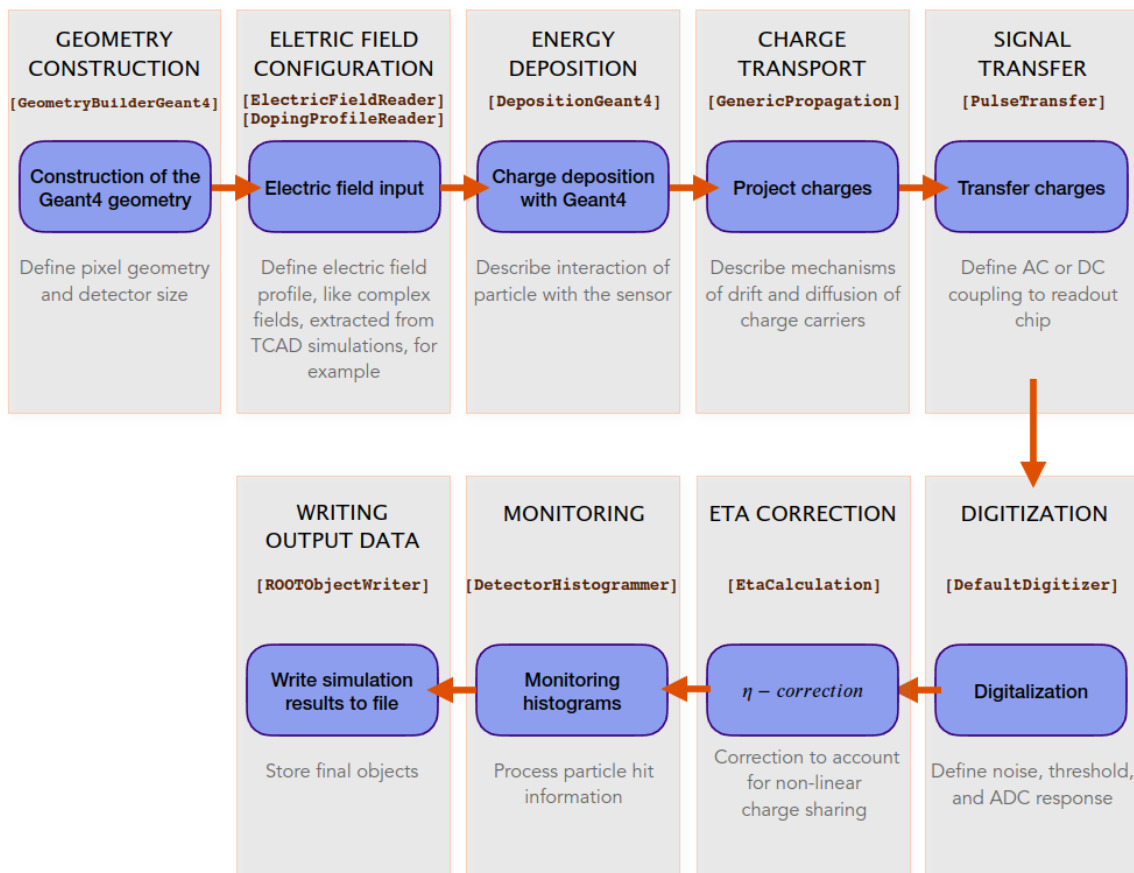


Figure 4.5: Typical simulation flow with Allpix², which includes the names of the modules used.

- **Global parameters**

With the header [Allpix] it is possible to set global parameters such as detector geometry and detector model configuration files, the number of events, and the output file path and name. The code piece (Listing 4.4) is part of the simulation configuration file and should contain the following parameters:

- detectors_file:** geometry configuration file;
- model_path:** model configuration file;
- multithreading:** running several events in parallel via its multithreading feature. By default, this feature is disabled;
- root_directory:** ROOT output data of all modules;
- random_seed:** Seed value to be used in seed module instantiations.
- number_of_events:** total number of events to simulate;

```

1 [Allpix]
2 detectors_file = "geometry.conf"
3 model_paths = "model.conf"
4 root_file = "modules_35um.root"
5 multithreading = true
6 random_seed = 24
7 number_of_events = 500000

```

Listing 4.4: simulation_ETAcac.conf (part 1)

- **Construction of the Geant4 geometry**

First, the GeometryBuilderGeant4 module provides an interface to Geant4 to create the geometry. The world_material is set to air.

```

1 [GeometryBuilderGeant4]
2 world_material = "air"

```

Listing 4.5: simulation_ETAcac.conf (part 2)

- **Electric field configuration**

The doping concentration and electric field values in the epitaxial layer are fed into Allpix² through the modules [ElectricFieldReader] and [DopingProfileReader] to guarantee higher accuracy of the sensor simulation. Using the Mesh Converter tool, the adaptive meshes are taken from 3D TCAD and transformed into regularly spaced grids to speed up the lookup of field values. The module parameters are:

model: type of the electric field or doping profile model;

file_name: name and location of the mesh file;

depletion_depth: the thickness of the depletion zone inside the sensor;

field_mapping: the electric field or doping profile is interpreted as a field spanning the full Euclidean angle and aligned on the center of the pixel unit cell, and field values are obtained with respect to the pixel center.

```

1 [ElectricFieldReader]
2 model = "mesh"
3 file_name = "field_ElectricField.apf"
4 depletion_depth = 10um
5 field_mapping = PIXEL_FULL
6
7 [DopingProfileReader]
8 model = "mesh"
9 file_name = "field_DopingConcentration.apf"
10 depletion_depth = 10um
11 field_mapping = PIXEL_FULL

```

Listing 4.6: simulation_ETAcalf.conf (part 3)

- **Energy deposition**

This module employs Geant4 to simulate the interactions between incident particles and the sensor. It is designed to simulate a particle source that deposits charge carriers during each event, using the mean pair creation [38] to calculate the number of electron-hole pairs created by a given energy deposition. Fluctuations are modeled through the use of a Fano factor that assumes Gaussian statistics.

For this thesis, the module is set up to simulate a 5 GeV electron beam, which is in line with typical test-beam measurements. To eliminate edge effects, the beam cross-section must be smaller than the sensor surface. The following parameters are used:

physics_list: Internal Geant4 list of physical processes to simulate [39];

number_of_particles: number of particles to be generated in a single event;

enable_pai: enable Photoabsorption Ionization Model (PAI) to improve the model describing the ionization energy loss produced by a relativistic charged particle in very thin materials [40]; .

particle_type: type of particle to use in the source;

source_energy: mean kinetic energy of the generated particle;

source_type: shape of the source;

- source_position:** location of the particle source in the world geometry;
- beam_size:** width of the Gaussian beam profile;
- beam_direction:** direction of the beam;
- beam_divergence:** Standard deviation of the particle angles in x and y directions;
- max_step_length:** maximum length of a simulation step.

```

1 [DepositionGeant4]
2 physics_list = QGSP_BERT_EMZ
3 enable_pai = 1
4 particle_type = "e-"
5 number_of_particles = 1
6 source_energy = 5GeV
7 source_position = 0um 0um -10mm
8 source_type = "beam"
9 beam_size = 100um
10 beam_divergence = 0mrad 0mrad
11 beam_direction = 0 0 1
12 max_step_length = 0.5um

```

Listing 4.7: simulation_ETAcalf.conf (part 4)

• Charge Transport

The [GenericPropagation] module simulates the propagation (drift and diffusion) of charge carriers through a sensor. The charge carrier mobility is calculated using the combined Masetti-Canali mobility model (see subsection 2.3.1), and the combined Shockley-Read-Hall and Auger recombination models are used to calculate the doping-dependent charge carrier lifetime. (see subsection 2.3.3).

This module utilizes a fourth-order Runge-Kutta-Fehlberg method with fifth-order error estimation to integrate particle propagation in electric and magnetic fields [41]. After each Runge-Kutta step, the diffusion effect is incorporated by applying an offset based on a Gaussian distribution. The parameters of this Gaussian distribution are determined using the Einstein relation, which captures the random motion and spreading of carriers due to diffusion.

$$\sigma = \sqrt{\frac{2k_b T}{e} \mu t} \quad (4.9)$$

where μ is the carrier mobility, T is the temperature and t is the step duration.

- temperature:** temperature of the sensitive device;
- mobility_model:** charge carrier mobility model;
- recombination_model:** charge carrier recombination model;

charge_per_step: maximum number of charge carriers that can propagate simultaneously;

timestep_min: minimum time step to employ for Runge-Kutta integration;

timestep_max: maximum time step to employ for Runge-Kutta integration;

integration_time: time span within which charge carriers propagate;

propagate_electrons: Choose if electron-type charge carriers should be transported to the electrodes.

```

1 [GenericPropagation]
2 temperature = 293K
3 mobility_model="masetti_canali"
4 recombination_model = "srh_auger"
5 charge_per_step = 5
6 timestep_min = 0.5ps
7 timestep_max = 0.05ns
8 integration_time = 25ns
9 propagate_electrons = true

```

Listing 4.8: simulation_ETAcalf.conf (part 5)

• ETA Calculation

In the `EtaCalculation` module, the distributions for two-pixel clusters are derived by comparing the in-pixel track position with the predicted cluster center position. Histograms are filled for both x and y coordinates, and fits of the recorded profiles are done at the end of each run using the specified equations. The final fit parameters are then used as input to the `[EtaCorrection]`.

chi2ndof_cut: track quality cut based on the ratio of χ^2 to the number of degrees of freedom;

eta_formula_x / eta_formula_y: formula for the recorded η – *distributions*

```

1 [EtaCalculation]
2 chi2ndof_cut = 100
3 eta_formula_x = [0] + [1]*x + [2]*x^2 + [3]*x^3 + [4]*x^4 + [5]*x^5

```

Listing 4.9: simulation_ETAcalf.conf (part 6)

• Signal Transfer

The final per-pixel current pulses are created by combining the currents caused by propagated charges at each individual pixel implant using the `PulseTransfer` module. This sets the pulse prepared for front-end electronics processing. These pulses are produced using the charge carrier arrival times at the pixel implants. The variables employed are:

max_depth_distance: maximum distance from which charge carriers are accepted;

collect_from_implant: chose if only consider charge carriers within the implant region instead of the full surface of the sensor;

```
1 [PulseTransfer]
2 max_depth_distance=0.55um
3 collect_from_implant = true
```

Listing 4.10: simulation_ETAcalc.conf (part 6)

• Digitization

The `DefaultDigitizer` module converts the charges collected into a digitized signal proportional to the input charge. It replicates noise contributions from the readout electronics as Gaussian noise and has a threshold. The parameters used in this module are:

electronics_noise: define the value of the standard deviation of the Gaussian noise in the electronics;

threshold: threshold energy level for considering the collected charge as a hit;

threshold_smearing: define the standard deviation of the Gaussian uncertainty in the threshold charge value.

```
1 [DefaultDigitizer]
2 electronics_noise = 10e
3 threshold = 200e
4 threshold_smearing = 5e
```

Listing 4.11: simulation_ETAcalc.conf (part 7)

• Monitoring data

For immediate analysis and easy inspections, the `[DetectorHistogrammer]` module offers an overview of the simulation data that was generated. It can provide details such as a hitmap of every pixel in the grid, a cluster map showing the positions of the clusters over the course of the whole simulation run, as well as an efficiency map.

name: name of the detector to plot;

output_plots: enable saving output plots;

track_resolution: track resolution the Monte Carlo truth is smeared with;

```

1 [DetectorHistogrammer]
2 name = "detector"
3 output_plots = 1
4 track_resolution = 0um 0um
5 granularity = 100, 100

```

Listing 4.12: simulation_ETAcalf.conf (part 8)

granularity: number of bins along the x and y axis for in-pixel maps.

- **Writing output data**

The simulation information can be stored in ROOT objects for external analysis with the `ROOTObjectWriter` module.

```

1 [ROOTObjectWriter]
2 file_name = "data.root"

```

Listing 4.13: simulation_ETAcalf.conf (part 9)

Simulation configuration part 2: Eta Correction

In this simulation step, the results from the eta calculation can be imported and final plots are created. Initially, the global parameters such as number of events and input files are set through `[AllPix]`, then `[ROOTObjectReader]` reads all trees defined in the input data file (`file_name`) that contain `Allpix2` objects.

The fit parameters are then used as input to the `[DetectorHistogrammer]` module. The configuration file allows separate specifications of the correction function and parameters for each detector along the x and y dimensions. The parameters for this module are:

name: name of the detector to plot;

eta_correction_function_*: the formula for the η – correction to be applied for the x and y coordinates and for polar coordinates;

eta_correction_parameters_*: vector of correction factors, representing the parameters of the above correction function, in x and y coordinates and for polar coordinates;

granularity: number of bins along the x and y axis for in-pixel maps.

```
1 [AllPix]
2 number_of_events = 100000
3 detectors_file = "geometry.conf"
4 model_paths="model.conf"
5 random_seed=24
6 root_file = "output_eta_correction_plots.root"
7 multithreading = true
8
9 [ROOTObjectReader]
10 file_name = "input_eta_calcutation_data.root"
11
12 [DetectorHistogrammer]
13 name = detector
14 eta_correction_function_x = "[0]+[1]*x+[2]*x^2+[3]*x^3+[4]*x^4+[5]*x^5"
15 eta_correction_parameters_x = 0.000155138 0.314214 60.0992 364.709 -3.51545 4.277
16 eta_correction_function_y = "[0]+[1]*x+[2]*x^2+[3]*x^3+[4]*x^4+[5]*x^5"
17 eta_correction_parameters_y = 7.08422e-05 0.393339 32.8107 -202 -1.72 4.0
18 eta_correction_function_2r = "[0]+[1]*x+[2]*x^2+[3]*x^3+[4]*x^4+[5]*x^5"
19 eta_correction_parameters_2r = -0.00651 10.0792 -2908.24 400702 -2.598 6.399
20 eta_correction_function_3r = "[0]+[1]*x+[2]*x^2+[3]*x^3+[4]*x^4+[5]*x^5"
21 eta_correction_parameters_3r = 0.0116617 -2.00828 280.965 -1474.86 -1.30 4.1057
22 eta_correction_function_3phi = "[0]+[1]*x+[2]*x^2+[3]*x^3+[4]*x^4+[5]*x^5"
23 eta_correction_parameters_3phi = -0.0422413 0.259477 0.999121 -3.24576 -1.79364 23.0009
24 granularity = 100, 100
```

Listing 4.14: simulation_ETAlc.conf (part 9). The eta_correction_parameters presented are an example. The correct values will be provided by the previous simulation step.

Chapter 5

Simulation Results and Discussions

This chapter presents the results of the study, along with their corresponding assessments. Similar to the previous chapter, it is divided into two parts: electrostatic simulations using TCAD and MC simulations with Allpix², where the TCAD meshes are utilized as input. In this work, simulations for hexagonal pixels were conducted for MAPS in two variations: standard process and n-gap, with pixel pitches of 35 μm and 18 μm , respectively. The 35 μm simulations aimed at validating the general behavior of hexagonal pixels, while the 18 μm size was used for a comparison between square and hexagonal pixels.

As discussed in Section 3.2, a single-pixel cell is employed to model the electrostatic field in the epitaxial layer of the sensor using a 3D TCAD simulation. In the Allpix² simulations, a full-size detector with dimensions of 100 x 100 pixels was considered, and periodic boundary conditions were applied to replicate the field across the entire sensor. This chapter presents the results of the doping and electric field profiles. Subsequently, the reconstruction and analysis of the MC events are discussed, where each simulation provides valuable information including cluster size, efficiency, pixel charge, and resolution.

5.1 Electrostatic Simulations

The 3D simulated structure is displayed in Figure 5.1. The x-direction is parallel to the apothem of the hexagon, the y-direction follows the y-pitch, and the z-direction follows the sensor depth. For reference, a two-dimensional cross-section indicated as *C1* in Figure 5.1, is shown in Figures 5.2 and 5.3 for pixel pitch of 18 μm and 35 μm , respectively.

The electric field strength in the pixel cell is depicted in Figures 5.4 and 5.5 within the pixel cell for pixel pitches of 18 μm and 35 μm , respectively, in both standard and n-gap sensor

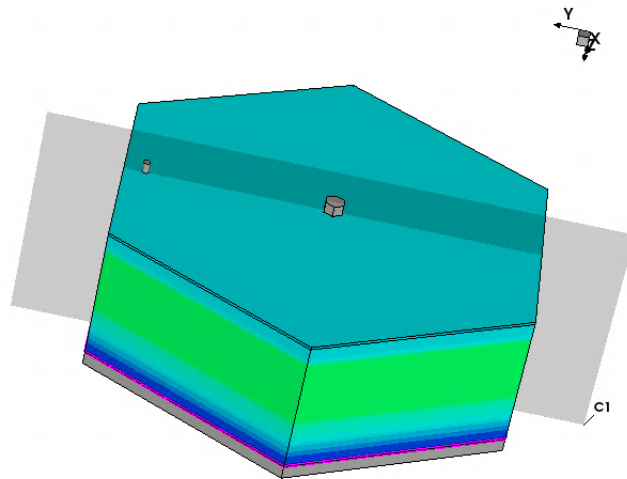


Figure 5.1: The 3D simulated structure for standard process simulation for pitch size of $35 \mu\text{m}$. The collection electrode is located at the center of the structure.

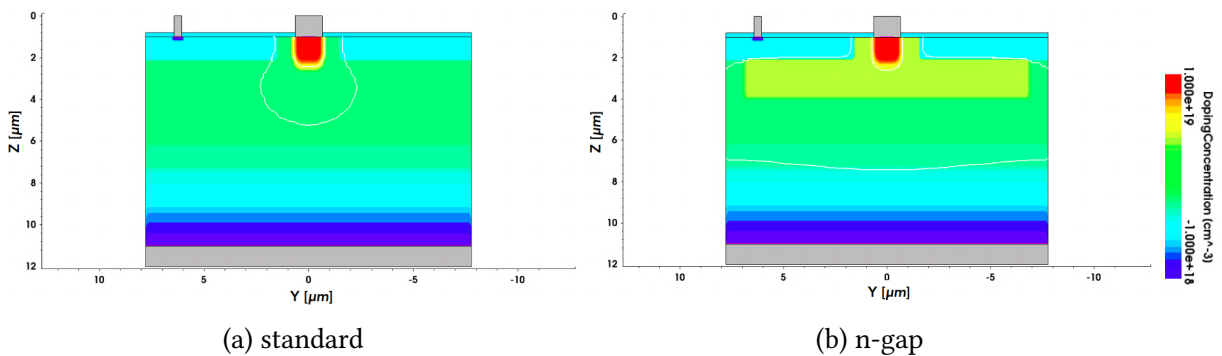


Figure 5.2: Doping concentrations results from the electrostatic simulation for (a) standard and (b) n-gap layouts for pixel pitch $18 \mu\text{m}$. The white lines indicate the boundary of the depleted volume, and the gray structures represent the corresponding terminals where voltages were applied via metal contacts.

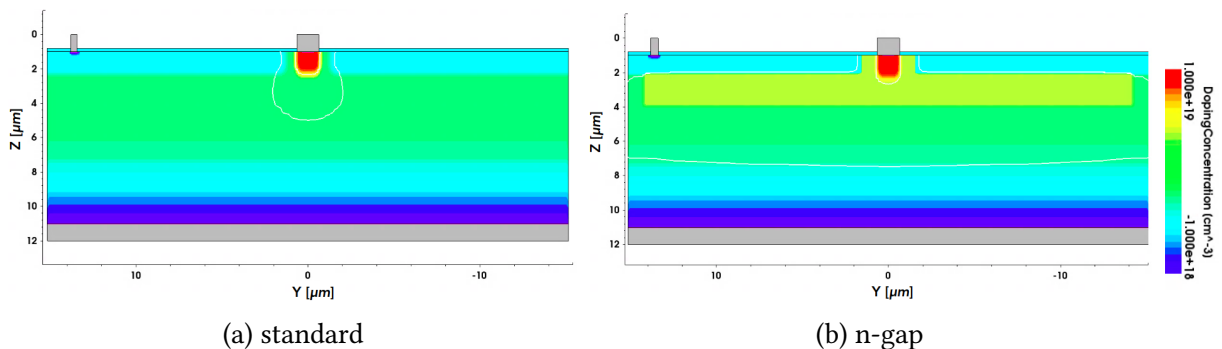


Figure 5.3: Doping concentrations results from the electrostatic simulation for (a) standard and (b) n-gap layouts for pixel pitch $35 \mu\text{m}$.

configurations. It can be observed that in the n-gap flavors, the inclusion of a continuous low-dose deep n-implant beneath the p-wells results in complete lateral depletion in the epitaxial layer.

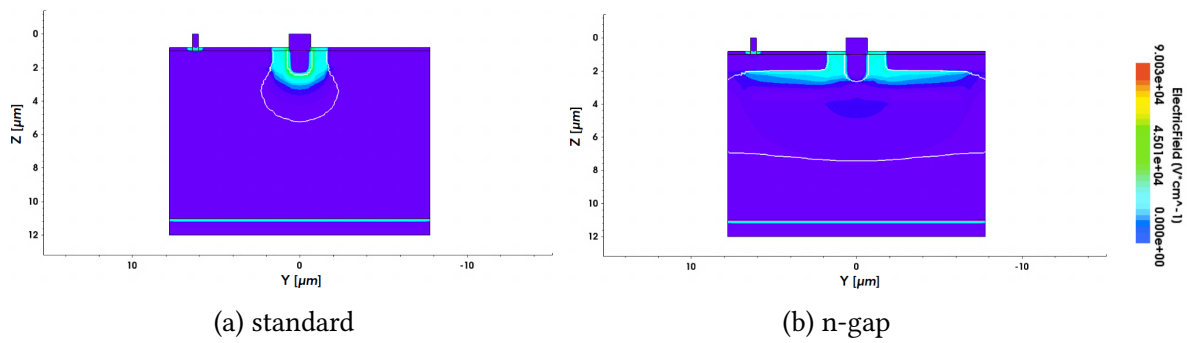


Figure 5.4: Electric field strength results from the electrostatic simulation for (a) standard and (b) n-gap layouts for pixel pitch $18 \mu m$. The white lines indicate the boundary of the depleted volume.

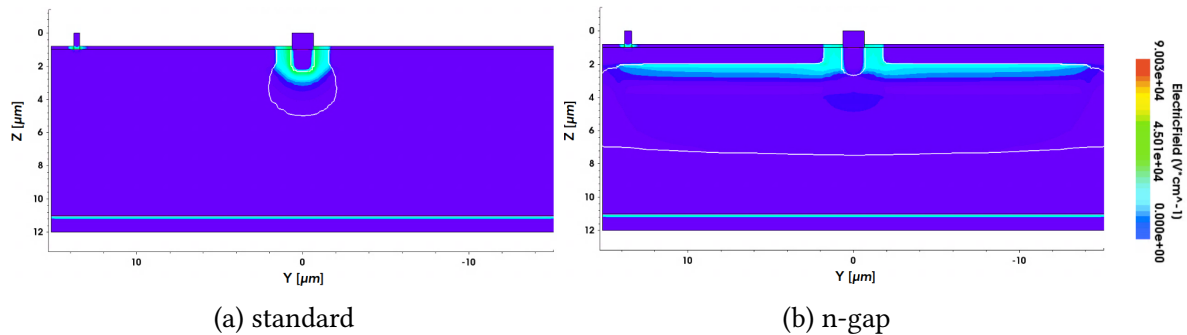


Figure 5.5: Electric field strength results from the electrostatic simulation for (a) standard and (b) n-gap layouts for pixel pitch $35 \mu m$.

The lateral electric field strength in the pixel cell is depicted in Figures 5.6 and 5.7 for pixel pitches of $18 \mu m$ and $35 \mu m$, respectively, in both standard and n-gap sensor configurations. As mentioned in section 3.1, the n-gap model incorporates a separation between the n-implant and the pixel edges, resulting in a distinct lateral electric field concentrated at the edges of the sensor, beneath the wells.

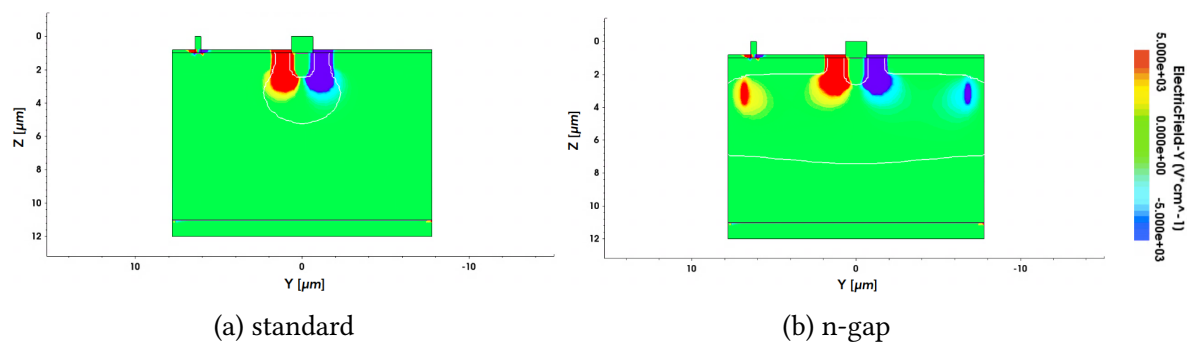


Figure 5.6: Lateral electric field strength for (a) standard and (b) n-gap layouts for pixel pitch $18 \mu m$. The white lines indicate the boundary of the depleted volume.

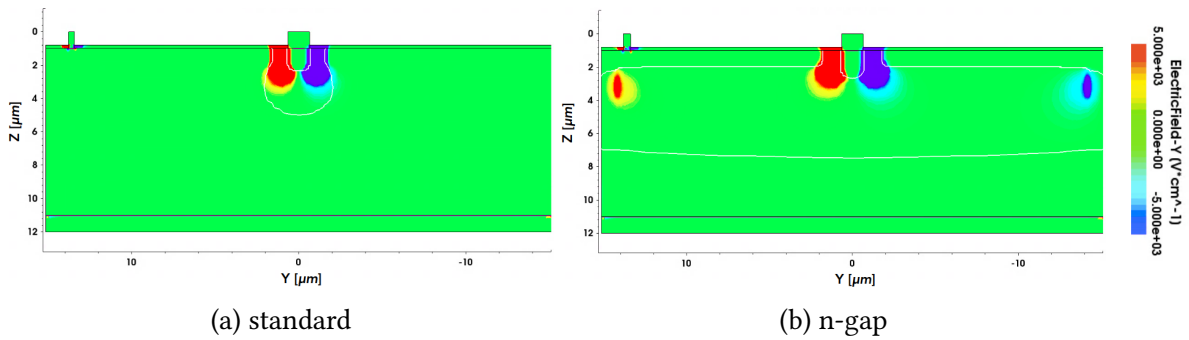


Figure 5.7: Lateral electric field strength for (a) standard and (b) n-gap layouts for pixel pitch $35 \mu\text{m}$. The white lines indicate the boundary of the depleted volume.

5.2 Monte Carlo Simulations

To extract data information from the detector, the hexagonal pixel simulation using Allpix² was conducted, utilizing the TCAD electric field and doping profiles described in the previous section. These profiles were imported as outlined in Section 4.1.1. Figure 5.8 visualizes the detector configuration in Geant4, where ten 5 GeV single-electron events are shown crossing the sensor (indicated by red arrows) and hitting the sensor (represented by the grey box). It is important to note that for each simulation, approximately 500,000 events were simulated to ensure reliable statistics.

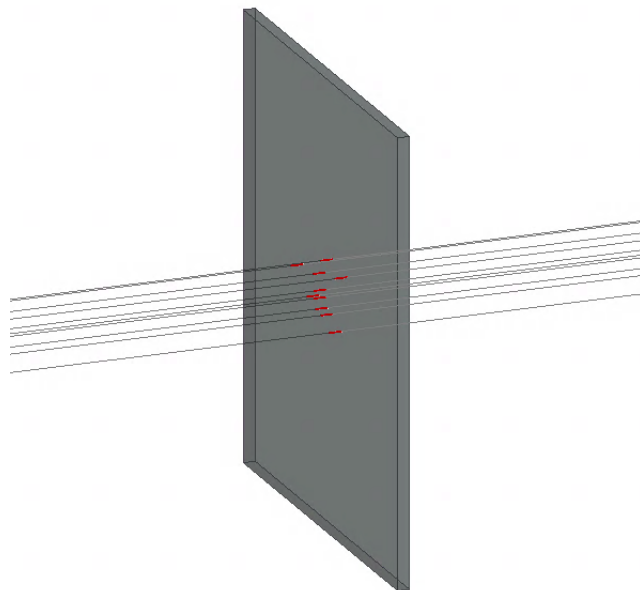


Figure 5.8: Geant4 visualization of the simulated detector (grey box). Ten 5 GeV single-electron events cross the sensor (red arrows). The visualization is obtained with the [VisualizationGeant4] module in Allpix².

Figure 5.9 shows line graphs illustrating the collection of charge carriers as a function of their position within the sensor in a random event. The x-axis represents the position between two collection electrodes, which are highlighted by red arrows. A single 5 GeV electron event originating near the center between these two electrodes is indicated by the black arrow. The vertical axis represents the sensor depth, with a distinction between the substrate and the epitaxial layer, which ends approximately $25 \mu\text{m}$ from the top of the sensor.

Figures 5.9a and 5.9b reveal that the majority of charges generated in the substrate undergo recombination within the silicon lattice. The motion paths of groups of charge carriers reaching the implant exhibit significant contributions from diffusion, as indicated by the curved trajectories. On the other hand, straight lines imply that the movement of charges is primarily governed by drift. In the standard layout, charges are collected in the epitaxial layer mostly through diffusion, while in the n-gap layout, charges are predominantly collected through drift, resulting in a more linear trajectory for collected electrons in the epitaxial layer.

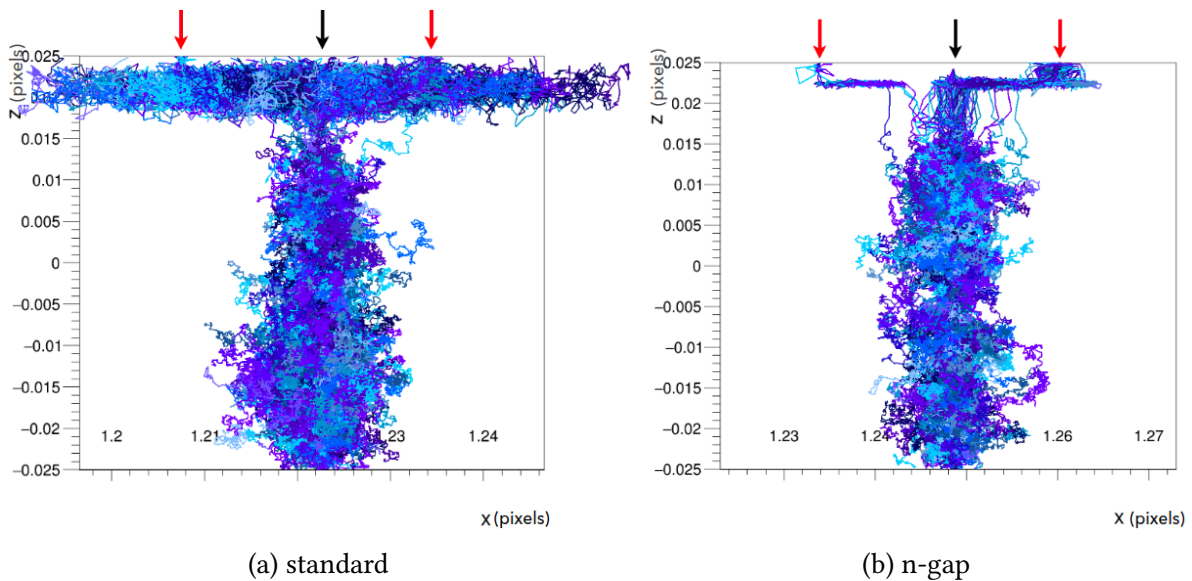


Figure 5.9: Line graphs for standard (a) and n-gap (b) layouts. The ionizing particle (with the initial position indicated by the black arrow) cross the sensor along the z-axis between two adjacent pixels (with collection electrodes indicated by red arrows).

5.2.1 Cluster Size

In a pixel detector, a cluster refers to a group of neighboring pixels that have been activated by the passage of a charged particle. The mean cluster size represents the average number of particles in each cluster.

The relationship between cluster size and charge sharing in a MAPS is similar to that in other types of pixel detectors. A larger cluster size can lead to a higher degree of charge sharing, making it more challenging to determine the precise position and energy of the particle that caused the cluster. Conversely, a smaller mean cluster size can result in less charge sharing, improving the accuracy of the reconstructed position and energy.

The mean cluster size in MAPS is influenced by the energy threshold setting. The energy threshold determines the minimum amount of energy required for a pixel to be considered part of a cluster. Generally, decreasing the energy threshold will increase the mean cluster size, as more low-energy particles are detected and contribute to larger clusters. However, the specific relationship between the mean cluster size and energy threshold value depends on factors such as the pixel design and shape (e.g., square or hexagonal).

To analyze the distribution of cluster sizes, an in-pixel representation is used. Figures 5.10 and 5.11 illustrate the cluster size distribution within a single pixel cell, obtained by folding the data from the entire pixel matrix (100 x 100 pixels) into a single representation. Allpix² collects the charge information from a defined region or cell within the full pixel matrix and calculates the total cluster size. By repeating this process for multiple events, the cluster size distribution within the condensed region can be analyzed. In this representation, the cluster size is plotted as a function of the incident position of the particle within the pixel cell. It is observed that the largest clusters tend to occur in the pixel corners, where the electric field is lower, leading to a significant contribution from charge carrier diffusion.

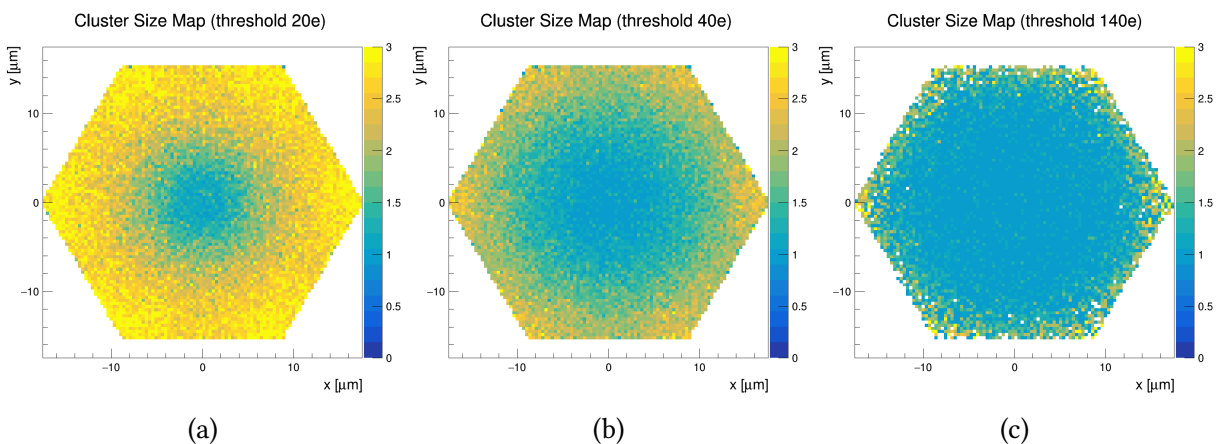


Figure 5.10: In-pixel representation of the cluster size for simulation at the threshold of (a) 20e, (b) 40e, and (c) 140e for a pixel size of 35 μm for standard layout.

The impact of the energy threshold on cluster size can be observed in the cluster size distribution shown in Figure 5.12, specifically for the simulation with a pitch size of 35 μm . Com-

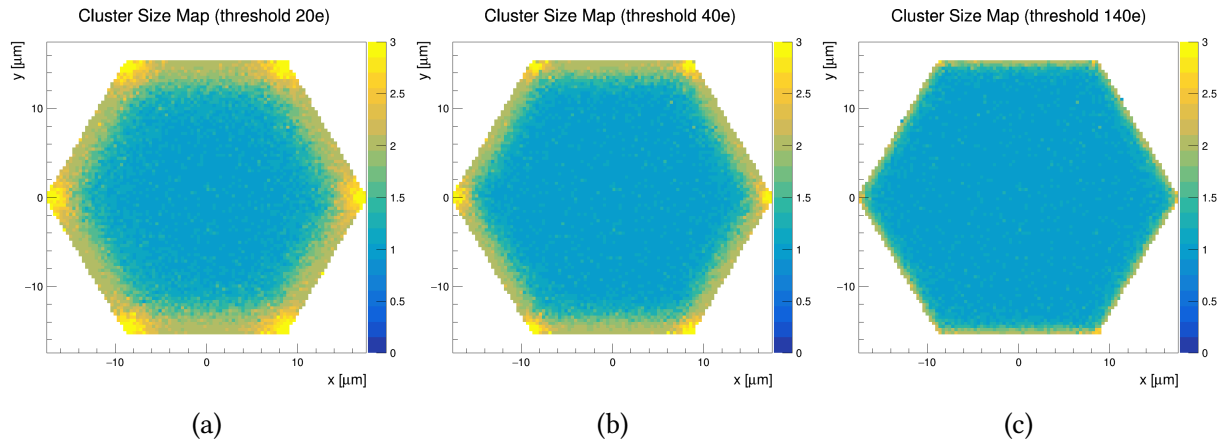


Figure 5.11: In-pixel representation of the cluster size for simulation at the threshold of (a) 20e, (b) 40e, and (c) 140e for a pixel size of $35 \mu m$ for n-gap layout.

paring the standard and n-gap models, it is evident that the n-gap model exhibits a narrower distribution and smaller cluster sizes.

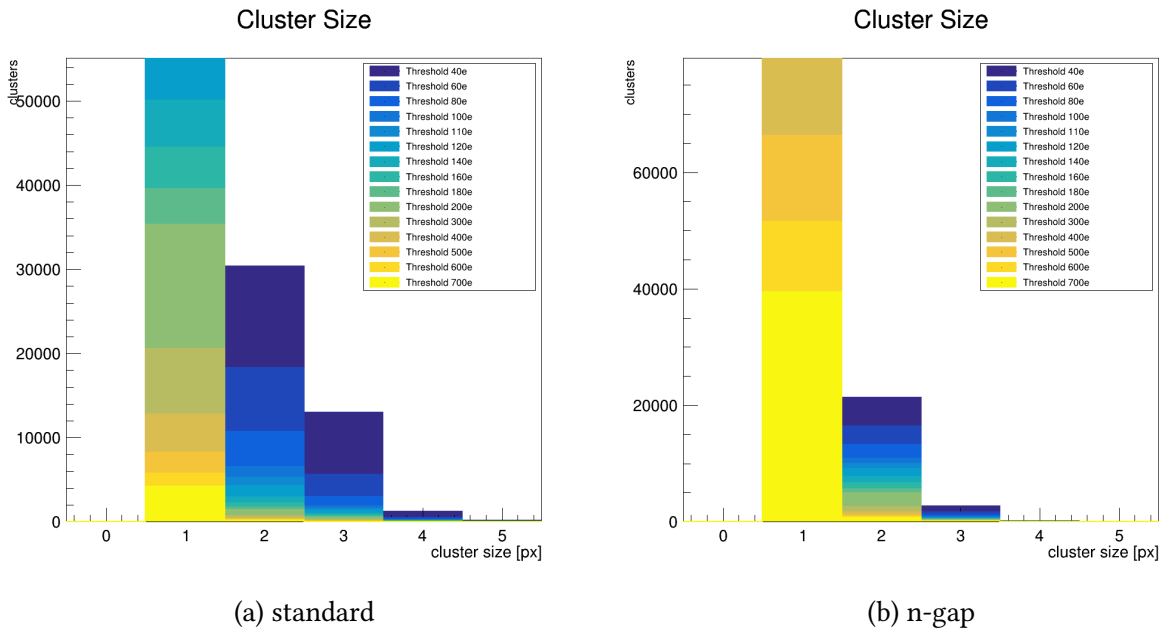


Figure 5.12: Cluster size histogram for multiple thresholds for standard layout (a) and n-gap layout (b).

A more interesting approach to analyzing the data is by calculating the average histogram value for each energy threshold. This method shows the relationship between the energy threshold and the mean cluster size. In Figure 5.13, the mean cluster size is plotted as a function of the energy threshold for a pixel size of $35 \mu m$.

In summary, regardless of the pixel geometry, the n-gap layout generally exhibits less charge sharing compared to the standard layout. This is attributed to differences in the col-

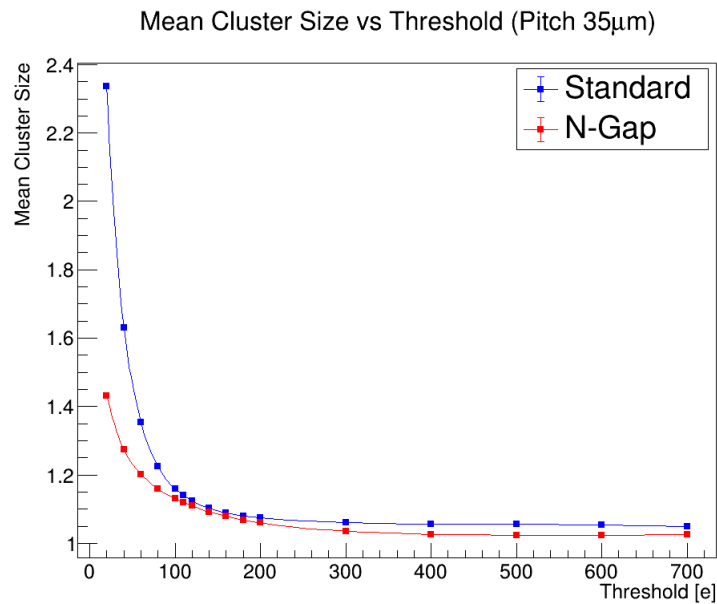


Figure 5.13: Mean cluster size as a function of the energy threshold for the pixel size of $35 \mu m$. Statistical errors in the simulation results are small due to a large number of simulated events (500,000 per configuration)

lection of charge carriers, influenced by the size of the depleted region and the lateral electric field in MAPS.

The Tangerine project is currently investigating the use of 65 nm CMOS imaging with MAPS featuring small collection electrodes. Ongoing activities involve sensor simulations, laboratory characterization, and test beam measurements using the first test chip with a square geometry [6, 42, 43]. As part of this thesis, simulation results have been provided for a square pixel with a pitch of $14.5 \mu m$. The characteristics of the square pixel, such as implant and p-well sizes, doping concentrations, depth sizes, and applied voltages, are similar to those of the hexagonal pixel. Figure 5.14 displays the mean cluster size distribution for square and hexagonal pixels, considering approximately the same area, with pitches of $14.5 \mu m$ and $18 \mu m$, respectively. The pitch definitions were presented in section 3.2.

Comparing hexagonal and square pixels with the same area is a common approach as it enables an accurate assessment of the total number of pixels and the overall detector performance. By maintaining the same area, the comparison takes into account factors such as the total amount of material used in the detector, which affects efficiency and resolution, as well as the capacity to accommodate electronics within the sensor.

For lower thresholds, Figure 5.14 shows that the square and hexagonal pixels with n-gap layout exhibit similar results. However, for higher thresholds, the charge released in a square

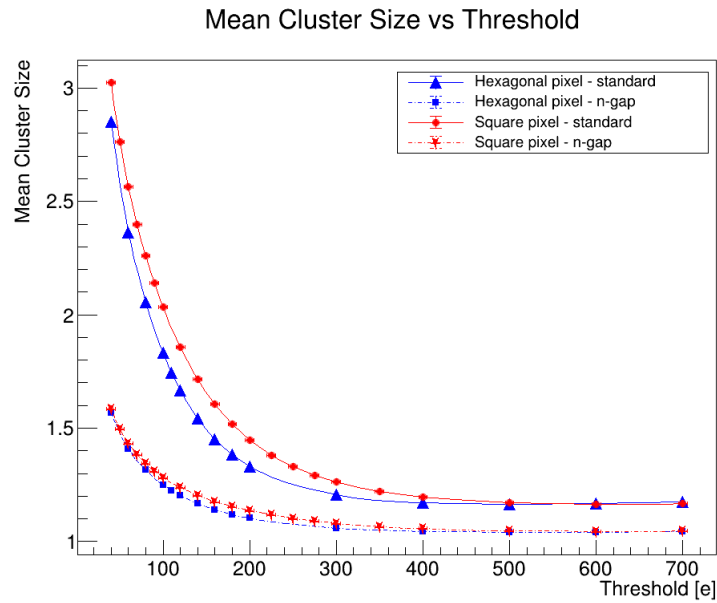


Figure 5.14: Mean cluster size as a function of the energy threshold for square and hexagonal pixel with approximately the same area, with pitch $14.5 \mu\text{m}$ [44] and $18 \mu\text{m}$, respectively.

pixel tends to spread out to more neighboring pixels compared to the hexagonal pixel, resulting in larger cluster sizes.

The reduction in mean cluster size for the n-gap layout is more pronounced for both pixel geometries, aligning with the expected decrease in charge sharing for this layout. However, in the case of the n-gap layout, the difference in cluster size between the two geometries is negligible. This is because the n-gap design limits the spread of charge in the sensor layer by increasing the electric field around the collection electrode, thereby already mitigating charge sharing and cluster size.

5.2.2 Detection Efficiency

The detection efficiency in MAPS refers to the proportion of particles that are successfully detected and recorded by the sensor. In MC simulations, this efficiency can be calculated by comparing the number of particles generated in the simulation to the number of particles that are detected and recorded by the sensor. Ideally, a high detection efficiency close to one indicates that all particle tracks are accurately captured.

In addition to the detector geometry, the detection efficiency is significantly influenced by the threshold. When a uniform charge distribution is spread across multiple pixels, a high threshold can reduce the efficiency, particularly at the edges and corners of the pixels. This

effect can be observed in the in-pixel map representations in Figures 5.15 and 5.16.c, which depict the efficiency for standard and n-gap layouts, respectively.

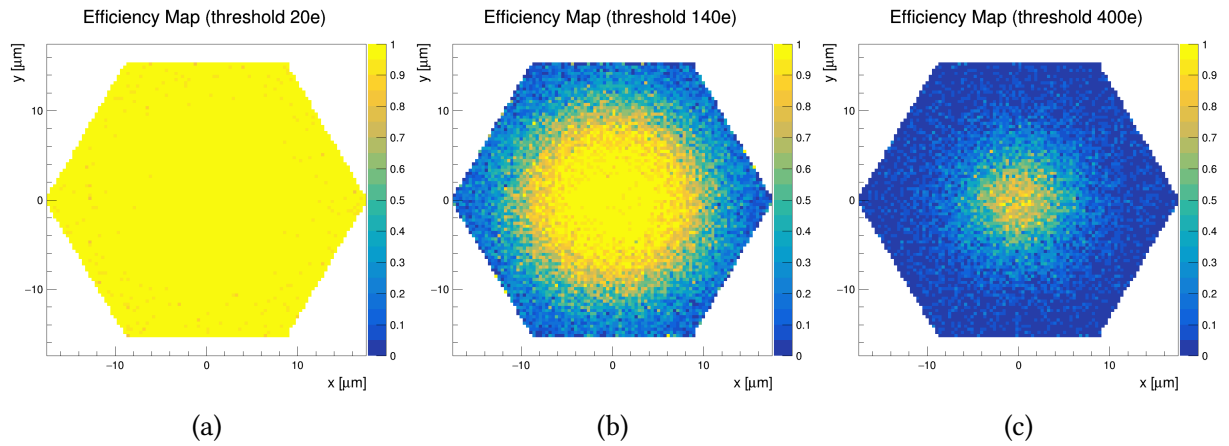


Figure 5.15: In-pixel representation of the efficiency at the threshold of (a) 20e, (b) 40e, and (c) 140e for a pixel size of $35 \mu\text{m}$ for standard layout.

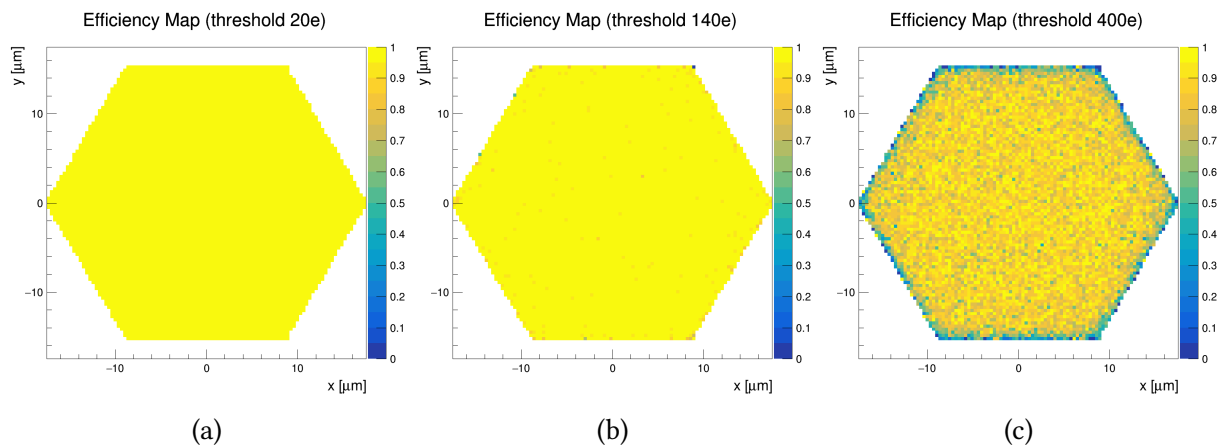


Figure 5.16: In-pixel representation of the efficiency at the threshold of (a) 20e, (b) 40e, and (c) 140e for a pixel size of $35 \mu\text{m}$ for n-gap layout.

The mean efficiency across the sensor for the standard and n-gap layouts is depicted in Figure 5.17. This metric is derived by computing the average map value for each threshold setting. The results confirm that the n-gap layout presents higher efficiency values across a broader range of thresholds compared to the standard layout.

To further explore the efficiency comparison, Figure 5.18 compares the mean efficiency distribution for square and hexagonal pixels with approximately the same area. Similar to the cluster size, the results reveal the higher efficiency achieved with the n-gap layout in both pixel geometries compared to the standard layout. However, it is noteworthy that the hexagonal pixel did not demonstrate substantial improvements in efficiency compared to the square

pixel with the n-gap layout. This could suggest that while the hexagonal pixel offers benefits in certain areas, it may not yield significant efficiency gains compared to the n-gap layout implemented in a square pixel configuration. Further investigations are required to validate and confirm these results.

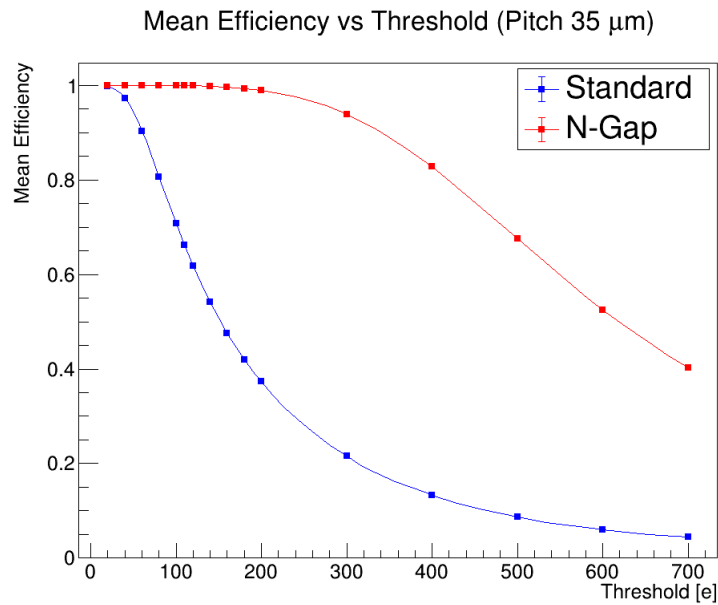


Figure 5.17: Mean efficiency as a function of the energy threshold for the pixel size of $35 \mu\text{m}$

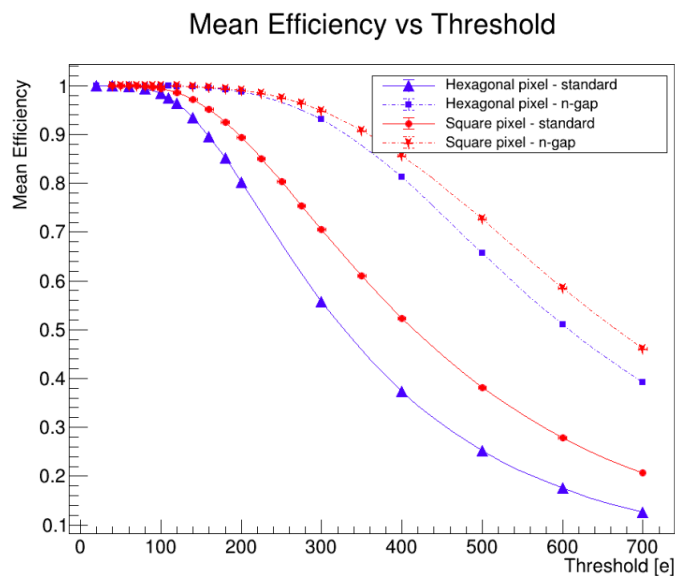


Figure 5.18: Mean efficiency as a function of the energy threshold for a square and a hexagonal pixel with approximately the same area, with pitch $14.5 \mu\text{m}$ [44] and $18 \mu\text{m}$, respectively.

5.2.3 Spatial Resolution

Spatial resolution in a tracking detector refers to the precision with which the detector can accurately determine the true position of a particle. It is commonly quantified by the square root of the variance of a probability function that describes the likelihood of detecting a particle signal at any given position x , having crossed the detector at x' . In MC simulations, the spatial resolution can be assessed using the spatial residual, which represents the difference between the reconstructed position of a particle and its expected position.

In the context of the *eta* correction process (see section 4.3.1), the residual histograms are fitted using a fifth-order polynomial, and the data is analyzed in polar coordinates ϕ and r , as depicted in Figure 5.19. This approach is particularly useful when assuming circular symmetry, simplifying the analysis of the data.

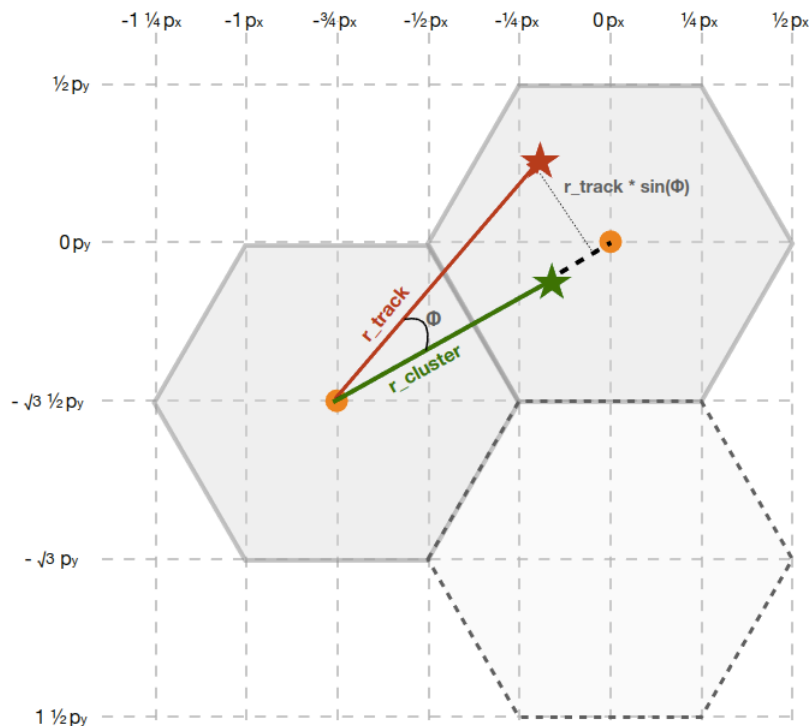


Figure 5.19: Coordinates used to calculate the residuals in polar coordinates, where r_{track} is the MC position of the incoming particle, and $r_{cluster}$ is the reconstructed cluster position in polar coordinates.

To compute the residuals in polar coordinates, a reference point is established at the center of the leftmost pixel in a two-pixel cluster. The residuals in the radial (r) direction are obtained by subtracting the reconstructed cluster position ($r_{cluster}$) from the MC position of the incoming particle (r_{track}), as $r_{track} - r_{cluster}$. Similarly, the residuals in the azimuthal (ϕ) direction are calculated as $r_{track} \cdot \sin(\phi)$.

Figures 5.21 and 5.20 illustrate the residuals before and after the *eta* correction, respectively. The *eta* correction significantly improves the distribution of residuals, resulting in a more accurate representation of the particle's true position. In x-y coordinates, the residuals are computed as the difference between the MC position and the reconstructed position.

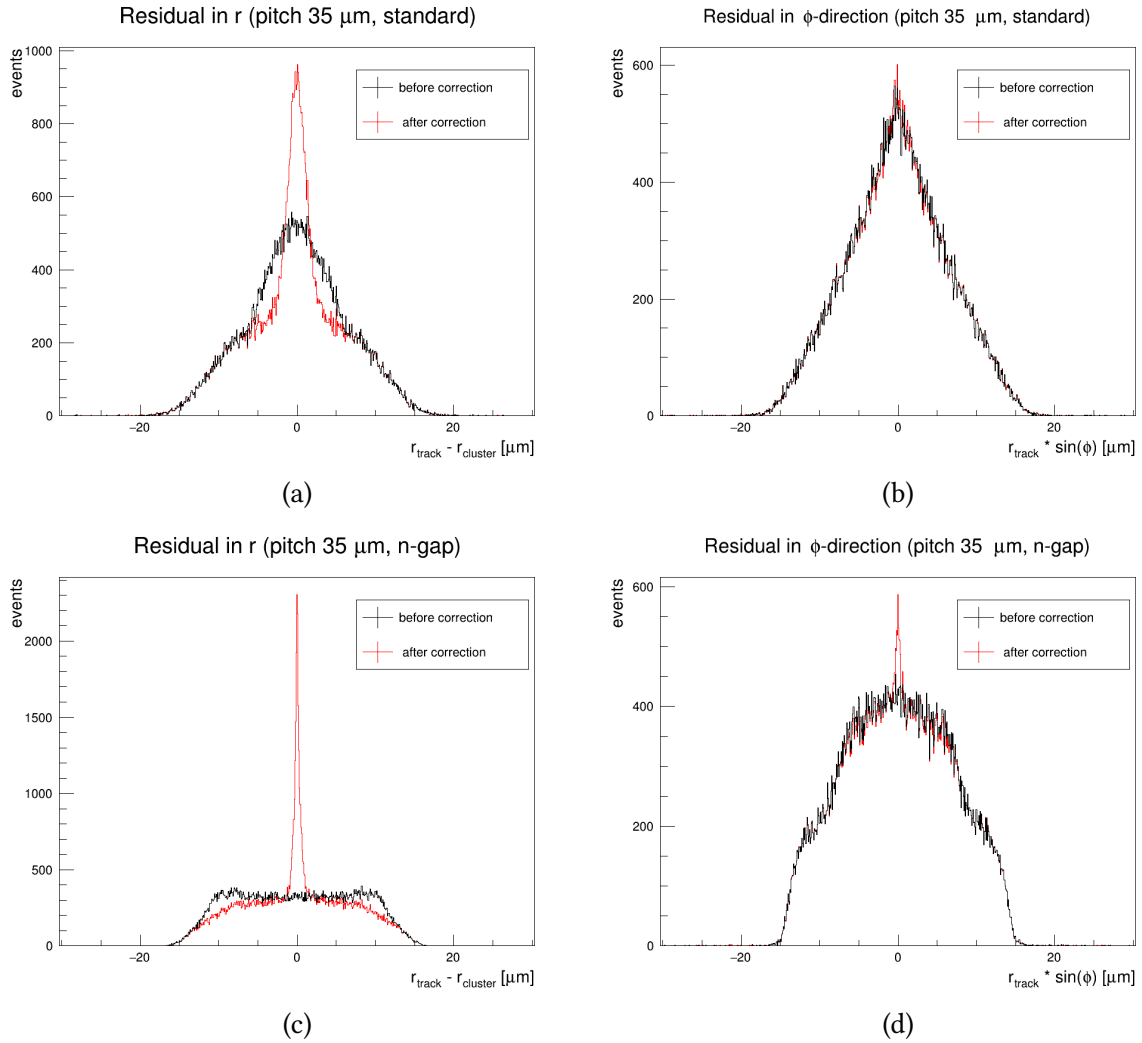


Figure 5.20: Residual histograms before and after *eta* correction for pixel pitch $35 \mu\text{m}$. Histograms acquired at threshold $60e$.

In this work, the spatial resolution is determined by calculating the root mean square of the central 99.73% (i.e., central 3σ) of the residual distribution. Since the simulated pixels are regular hexagons, the spatial resolution is found to be similar in both polar (r and ϕ directions) and x-y coordinates.

Figure 5.22 shows the spatial resolution for the two different layouts in both polar and x-y coordinates. A lower value indicates a higher resolution, indicating better precision in determining the true position of the particle.

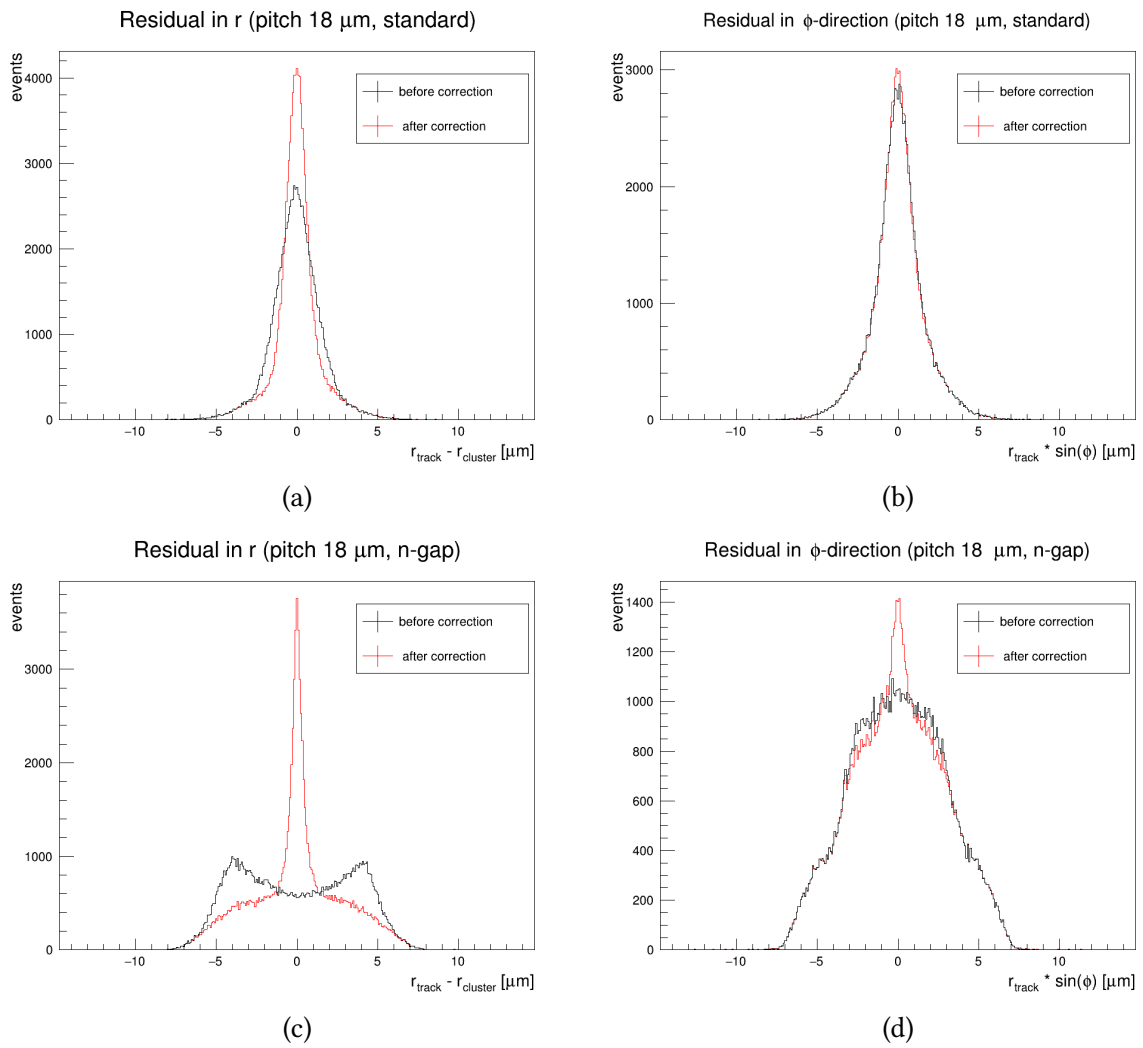


Figure 5.21: Residual histograms before and after *eta* correction for pixel pitch 18 μm . Histograms acquired at threshold 60e.

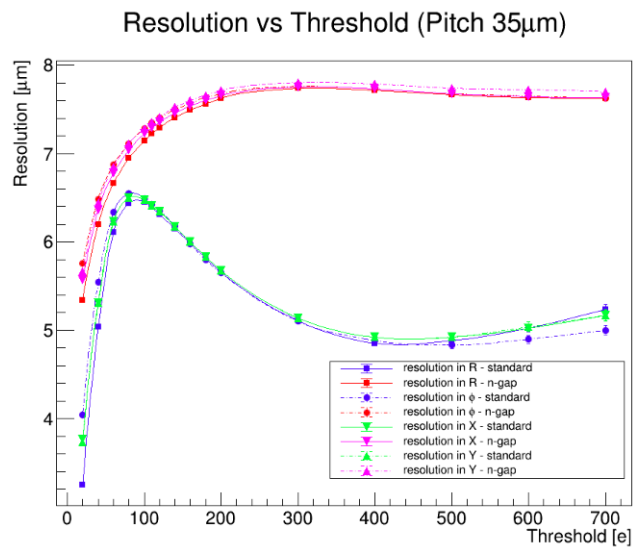


Figure 5.22: Spatial resolution as a function of the energy threshold for the pixel size of 35 μm .

It can be observed that the standard layout offers higher resolution, enabling more precise particle position measurements. This is because a sensor with a bigger cluster size provides a more precise reconstructed position due to charge-weighted interpolation between more pixels. In the standard layout, the presence of a larger undepleted zone at the borders of the pixels leads to increased charge diffusion and dispersion to neighboring pixels, resulting in larger cluster sizes. Conversely, the n-gap layout is designed to promote charge transport towards the collecting electrodes, minimizing charge sharing and yielding lower spatial resolution.

Furthermore, a comparison between a square pixel and a hexagonal pixel of approximately the same area is performed, as depicted in Figure 5.23. In both geometries, the standard layout consistently outperforms the n-gap layout in terms of resolution, and hexagonal pixels provide higher spatial resolution.

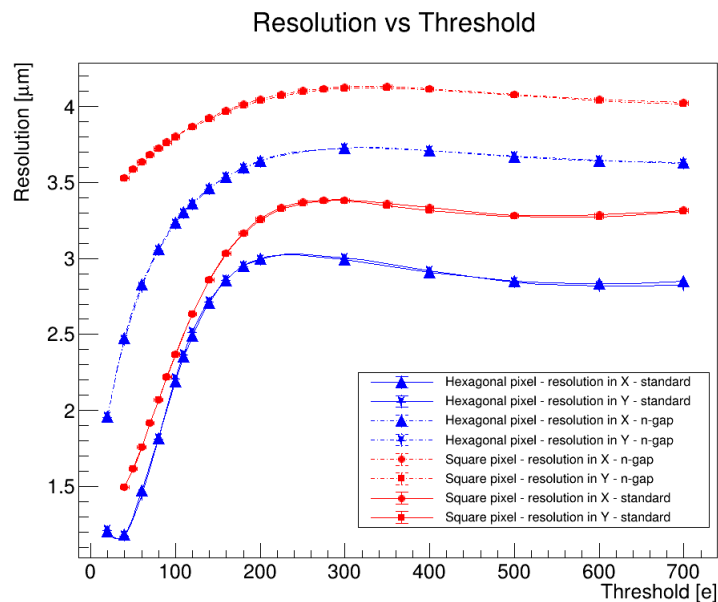


Figure 5.23: Spatial resolution as a function of the energy threshold for square and hexagonal pixel with approximately the same area, with pitch $14.5 \mu\text{m}$ [44] and $18 \mu\text{m}$, respectively.

Chapter 6

Conclusions

HEP experiments extend the knowledge of fundamental properties of nature, employing multi-purpose detectors. To meet the demands of modern and future colliders, Monolithic Active Pixel Sensors (MAPS) have been developed, offering high spatial resolution, efficiency, and low power consumption. One notable project in this field is the Tangerine Project, which aims to develop new silicon detectors for potential use in future lepton or electron-ion colliders. The performance goals of the new sensor are a position resolution below $3 \mu\text{m}$, a time resolution finer than 10 ns, and a material budget less than 0.05% of radiation lengths[6].

In this study, the focus was on characterizing hexagonal pixels in MAPS 65 nm CMOS imaging technology, featuring a small collection electrode. To achieve this objective, detailed 3D electric field models generated from TCAD were integrated into Monte Carlo simulations using the Allpix² framework. Tangerine Project uses these simulations to validate detector response modeling, predict the performance of future prototypes, and understand charge carrier drift behavior.

For this work, two sensor layouts were simulated: standard and n-gap. The results indicate that the implementation of these layouts in hexagonal pixels was consistent with the sensor simulations conducted on square pixels with the same design [6, 42, 43]. The simulations were performed using a beam of 5 GeV electrons on a 100×100 sensor with a pixel size (pixel pitch) of $35 \times 35 \mu\text{m}^2$ and $18 \times 18 \mu\text{m}^2$. To assess the sensor performance, various figures of merit are employed, including detection efficiency, cluster size, and spatial resolution. By varying the detection threshold, these values were also plotted against the threshold value, enabling a comprehensive analysis of their behavior and characteristics.

The comparison of cluster size in the standard layout against the n-gap layout in hexagonal pixels verifies that the n-gap model displays an advantage in terms of mean cluster size. This translates into reduced charge sharing between pixels and smaller cluster sizes in n-gap MAPS.

In addition, the simulation compared square and hexagonal pixels with same areas. The results indicate that, for the standard layout, hexagonal pixels exhibit smaller cluster sizes compared to square pixels. However, for the n-gap layout, the difference in cluster size between the two geometries is negligible.

Conversely, in contrast to what was expected, the hexagonal pixel did not deliver better efficiency performance when comparing geometries. Further investigations need to be carried out to explore the differences between the two models. For instance, the size and shape of the collection electrodes, as well as the size of the p-well, are important factors that should be assessed.

The spatial resolution exhibits a noticeable decline as the threshold value increases. For hexagonal pixels with a $35 \mu\text{m}$ pitch, the standard layout achieves the highest resolution at approximately $3 \mu\text{m}$, while the n-gap layout slightly lags behind with a resolution of around $3.4 \mu\text{m}$. The higher resolution of the standard layout can be attributed to its larger cluster size, which allows for more accurate reconstruction of particle positions through charge-weighted interpolation across multiple pixels. Moreover, the standard layout's larger undepleted region near the pixel edges facilitates charge diffusion and spreading to neighboring pixels, further contributing to increased cluster size. These characteristics hold true for both square and hexagonal pixel geometries. However, when comparing the two geometries with the same area, simulations suggest that hexagonal pixels generally offer better resolution. Future investigations will explore potential adjustments in the detector model aimed at further enhancing performance.

Furthermore, this work was motivated by the purpose of exploring alternative strategies for future particle detectors and demonstrating the potential benefits of using hexagonal pixel geometries. To gain deeper insights, further investigations will be conducted to better compare the performance of square and hexagonal pixels, as well as to examine the impact of other parameters such as pixel size, and sensor layout modifications. These simulation studies are important in advancing our understanding of the various factors affecting detector efficiency and spatial resolution, with the ultimate goal of identifying a combination of characteristics that can deliver optimal performance with a low detection threshold.

Bibliography

- [1] Norbert Wermes and G Hallewel. *ATLAS pixel detector: Technical Design Report*. Technical design report. ATLAS. Geneva: CERN, 1998. URL: <https://cds.cern.ch/record/381263>.
- [2] V Karimäki et al. *The CMS tracker system project: Technical Design Report*. Technical design report. CMS. Geneva: CERN, 1997. URL: <https://cds.cern.ch/record/368412>.
- [3] *ALICE Inner Tracking System (ITS): Technical Design Report*. Technical design report. ALICE. Geneva: CERN, 1999. URL: <https://cds.cern.ch/record/391175>.
- [4] T. Poikela et al. “VeloPix: the pixel ASIC for the LHCb upgrade”. In: *Journal of Instrumentation* 10 (Jan. 2015), pp. C01057–C01057. DOI: [10.1088/1748-0221/10/01/C01057](https://doi.org/10.1088/1748-0221/10/01/C01057).
- [5] N. Wermes. “Pixel detectors ... where do we stand?” In: *Nuclear Instruments and Methods in Physics Research Section A: Accelerators, Spectrometers, Detectors and Associated Equipment* 924 (2019). 11th International Hiroshima Symposium on Development and Application of Semiconductor Tracking Detectors, pp. 44–50. ISSN: 0168-9002. DOI: <https://doi.org/10.1016/j.nima.2018.07.003>. URL: <https://www.sciencedirect.com/science/article/pii/S016890021830826X>.
- [6] Håkan Wennlöf et al. “The Tangerine project: Development of high-resolution 65 nm silicon MAPS”. In: *Nuclear Instruments and Methods in Physics Research Section A: Accelerators, Spectrometers, Detectors and Associated Equipment* 1039 (2022), p. 167025. ISSN: 0168-9002. DOI: <https://doi.org/10.1016/j.nima.2022.167025>. URL: <https://www.sciencedirect.com/science/article/pii/S0168900222004508>.

- [7] W. Snoeys. “Monolithic pixel detectors for high energy physics”. In: *Nuclear Instruments and Methods in Physics Research Section A: Accelerators, Spectrometers, Detectors and Associated Equipment* 731 (2013). PIXEL 2012, pp. 125–130. ISSN: 0168-9002. DOI: <https://doi.org/10.1016/j.nima.2013.05.073>. URL: <https://www.sciencedirect.com/science/article/pii/S0168900213006840>.
- [8] N. Wermes. “Trends in pixel detectors: tracking and imaging”. In: *IEEE Transactions on Nuclear Science* 51.3 (2004), pp. 1006–1015. DOI: [10.1109/TNS.2004.829438](https://doi.org/10.1109/TNS.2004.829438).
- [9] Michele Selvaggi, Michelangelo Mangano, and Clement Helsens. *Requirements from physics for the FCC-hh detector design*. Tech. rep. Geneva: CERN, 2020. URL: <https://cds.cern.ch/record/2717785>.
- [10] A. Robson et al. *The Compact Linear e^+e^- Collider (CLIC): Accelerator and Detector*. 2018. DOI: [10.48550/ARXIV.1812.07987](https://doi.org/10.48550/ARXIV.1812.07987). URL: <https://arxiv.org/abs/1812.07987>.
- [11] H Abramowicz et al. “The International Large Detector at the International Linear Collider”. In: (Dec. 2019).
- [12] Hermann Kolanoski and Norbert Wermes. “Semiconductor detectors”. In: *Particle Detectors: Fundamentals and Applications*. Oxford University Press, June 2020. DOI: [10.1093/oso/9780198858362.003.0008](https://doi.org/10.1093/oso/9780198858362.003.0008). eprint: <https://academic.oup.com/book/0/chapter/365032187/chapter-pdf/46523969/oso-9780198858362-chapter-8.pdf>. URL: <https://doi.org/10.1093/oso/9780198858362.003.0008>.
- [13] Gerhard Lutz. *Semiconductor Radiation Detectors: Device Physics*. New York: Springer, 1999. ISBN: 978-3-540-64859-8.
- [14] Khaled S. Hameed Adnan M. AL-Sheikh. “Theoretical Study of Energy Gap for Silicon and Germanium Under High Pressure”. In: *Rafidain Journal of Science* 22.3 (2011), pp. 58–68. ISSN: 1608-9391. DOI: [10.33899/rjs.2011.31189](https://doi.org/10.33899/rjs.2011.31189). URL: https://rsci.mosuljournals.com/article_31189.html.
- [15] Glenn F. Knoll. *Radiation detection and measurement / Glenn F. Knoll*. English. 2nd ed. Wiley New York, 1989, xix, 754 p. : ISBN: 0471815047.

- [16] A. B. Sproul and M. A. Green. “Improved value for the silicon intrinsic carrier concentration from 275 to 375 K”. In: *Journal of Applied Physics* 70.2 (July 1991), pp. 846–854. ISSN: 0021-8979. DOI: [10.1063/1.349645](https://doi.org/10.1063/1.349645). eprint: https://pubs.aip.org/aip/jap/article-pdf/70/2/846/8020516/846_1_online.pdf. URL: <https://doi.org/10.1063/1.349645>.
- [17] Claus Grupen and Boris Shwartz. *Particle Detectors*. 2nd ed. Cambridge Monographs on Particle Physics, Nuclear Physics and Cosmology. Cambridge University Press, 2008. DOI: [10.1017/CBO9780511534966](https://doi.org/10.1017/CBO9780511534966).
- [18] R. L. Workman et al. “Review of Particle Physics”. In: *PTEP* 2022 (2022), p. 083C01. DOI: [10.1093/ptep/ptac097](https://doi.org/10.1093/ptep/ptac097).
- [19] C. Canali et al. “Electron and hole drift velocity measurements in silicon and their empirical relation to electric field and temperature”. In: *IEEE Transactions on Electron Devices* 22.11 (Nov. 1975), pp. 1045–1047. DOI: [10.1109/T-ED.1975.18267](https://doi.org/10.1109/T-ED.1975.18267).
- [20] C. Jacoboni et al. “A review of some charge transport properties of silicon”. In: *Solid-State Electronics* 20.2 (1977), pp. 77–89. ISSN: 0038-1101. DOI: [https://doi.org/10.1016/0038-1101\(77\)90054-5](https://doi.org/10.1016/0038-1101(77)90054-5). URL: <https://www.sciencedirect.com/science/article/pii/0038110177900545>.
- [21] G. Masetti, M. Severi, and S. Solmi. “Modeling of carrier mobility against carrier concentration in arsenic-, phosphorus-, and boron-doped silicon”. In: *IEEE Transactions on Electron Devices* 30.7 (1983), pp. 764–769. DOI: [10.1109/T-ED.1983.21207](https://doi.org/10.1109/T-ED.1983.21207).
- [22] W. Shockley and W. T. Read. “Statistics of the Recombinations of Holes and Electrons”. In: *Phys. Rev.* 87 (5 Sept. 1952), pp. 835–842. DOI: [10.1103/PhysRev.87.835](https://doi.org/10.1103/PhysRev.87.835). URL: <https://link.aps.org/doi/10.1103/PhysRev.87.835>.
- [23] Andres Cuevas. “The Recombination Parameter J_0 ”. In: *Energy Procedia* 55 (Dec. 2014). DOI: [10.1016/j.egypro.2014.08.073](https://doi.org/10.1016/j.egypro.2014.08.073).
- [24] J. Dziewior and W. Schmid. “Auger coefficients for highly doped and highly excited silicon”. In: *Applied Physics Letters* 31.5 (1977), pp. 346–348. DOI: [10.1063/1.89694](https://doi.org/10.1063/1.89694). eprint: <https://doi.org/10.1063/1.89694>. URL: <https://doi.org/10.1063/1.89694>.

- [25] Koen Wolters Paul Schütze Simon Spannagel. *Allpix² User Manual*. Version v2.3.3. <https://project-allpix-squared.web.cern.ch/usermanual/allpix-manual.pdf>, 2022.
- [26] Philip Allport. “Applications of silicon strip and pixel-based particle tracking detectors”. In: *Nature Rev. Phys.* 1.9 (2019), pp. 567–576. DOI: [10.1038/s42254-019-0081-z](https://doi.org/10.1038/s42254-019-0081-z).
- [27] Rafael Ballabriga et al. “Review of hybrid pixel detector readout ASICs for spectroscopic X-ray imaging”. In: *Journal of Instrumentation* 11 (Jan. 2016), P01007. DOI: [10.1088/1748-0221/11/01/P01007](https://doi.org/10.1088/1748-0221/11/01/P01007).
- [28] Thanushan Kugathasan et al. “Monolithic CMOS sensors for sub-nanosecond timing”. In: *Nuclear Instruments and Methods in Physics Research Section A: Accelerators, Spectrometers, Detectors and Associated Equipment* 979 (2020), p. 164461. ISSN: 0168-9002. DOI: <https://doi.org/10.1016/j.nima.2020.164461>. URL: <https://www.sciencedirect.com/science/article/pii/S0168900220308585>.
- [29] M. Munker et al. “Simulations of CMOS pixel sensors with a small collection electrode, improved for a faster charge collection and increased radiation tolerance”. In: *Journal of Instrumentation* 14.05 (May 2019), p. C05013. DOI: [10.1088/1748-0221/14/05/C05013](https://doi.org/10.1088/1748-0221/14/05/C05013). URL: <https://dx.doi.org/10.1088/1748-0221/14/05/C05013>.
- [30] W. Snoeys et al. “A process modification for CMOS monolithic active pixel sensors for enhanced depletion, timing performance and radiation tolerance”. In: *Nuclear Instruments and Methods in Physics Research Section A: Accelerators, Spectrometers, Detectors and Associated Equipment* 871 (2017), pp. 90–96. ISSN: 0168-9002. DOI: <https://doi.org/10.1016/j.nima.2017.07.046>. URL: <https://www.sciencedirect.com/science/article/pii/S016890021730791X>.
- [31] Yung-Chun Wu and Yi-Ruei Jhan. “Introduction of Synopsys Sentaurus TCAD Simulation”. In: *3D TCAD Simulation for CMOS Nanoelectronic Devices*. Singapore: Springer Singapore, 2018, pp. 1–17. ISBN: 978-981-10-3066-6. DOI: [10.1007/978-981-10-3066-6_1](https://doi.org/10.1007/978-981-10-3066-6_1). URL: https://doi.org/10.1007/978-981-10-3066-6_1.
- [32] Jan Hasenbichler. “Development of Novel Pixel CMOS Sensors Optimised for Time Resolution”. Presented 01 Sep 2021. 2021. URL: <https://cds.cern.ch/record/2806261>.

- [33] *Sentaurus™ Device User Guide*. Version K-2015.06. Synopsys, Inc. June 2015.
- [34] Jan W. Slotboom. “The pn-product in silicon”. In: *Solid-state Electronics* 20 (1977), pp. 279–283.
- [35] J.W. Slotboom and H.C. de Graaff. “Measurements of bandgap narrowing in Si bipolar transistors”. In: *Solid-State Electronics* 19.10 (1976), pp. 857–862. ISSN: 0038-1101. DOI: [https://doi.org/10.1016/0038-1101\(76\)90043-5](https://doi.org/10.1016/0038-1101(76)90043-5). URL: <https://www.sciencedirect.com/science/article/pii/0038110176900435>.
- [36] Christian Fabjan and Herwig Schopper. *Particle Physics Reference Library Volume 2: Detectors for Particles and Radiation: Volume 2: Detectors for Particles and Radiation*. Jan. 2020. ISBN: 978-3-030-35317-9. DOI: [10.1007/978-3-030-35318-6](https://doi.org/10.1007/978-3-030-35318-6).
- [37] S. Spannagel et al. “Allpix2: A modular simulation framework for silicon detectors”. In: *Nuclear Instruments and Methods in Physics Research Section A: Accelerators, Spectrometers, Detectors and Associated Equipment* 901 (2018), pp. 164–172. ISSN: 0168-9002. DOI: <https://doi.org/10.1016/j.nima.2018.06.020>. URL: <https://www.sciencedirect.com/science/article/pii/S0168900218307411>.
- [38] John J. Smithrick and Ira T. Myers. “Average Triton Energy Deposited in Silicon per Electron-Hole Pair Produced”. In: *Phys. Rev. B* 1 (7 Apr. 1970), pp. 2945–2948. DOI: [10.1103/PhysRevB.1.2945](https://doi.org/10.1103/PhysRevB.1.2945). URL: <https://link.aps.org/doi/10.1103/PhysRevB.1.2945>.
- [39] *Geant4 Collaboration*. <https://geant4-userdoc.web.cern.ch/UsersGuides/IntroductionToGeant4/html/index.html>. Accessed: 10-02-2022.
- [40] J Apostolakis et al. “An implementation of ionisation energy loss in very thin absorbers for the GEANT4 simulation package”. In: *Nuclear Instruments and Methods in Physics Research Section A: Accelerators, Spectrometers, Detectors and Associated Equipment* 453.3 (2000), pp. 597–605. ISSN: 0168-9002. DOI: [https://doi.org/10.1016/S0168-9002\(00\)00457-5](https://doi.org/10.1016/S0168-9002(00)00457-5). URL: <https://www.sciencedirect.com/science/article/pii/S0168900200004575>.
- [41] E. Fehlberg. “Low-order classical Runge-Kutta formulas with stepsize control and their application to some heat transfer problems”. In: 1969.

-
- [42] Ankur Chauhan et al. "Towards a new generation of Monolithic Active Pixel Sensors". In: *Nuclear Instruments and Methods in Physics Research Section A: Accelerators, Spectrometers, Detectors and Associated Equipment* 1047 (Feb. 2023), p. 167821. DOI: [10 . 1016 / j . nima . 2022 . 167821](https://doi.org/10.1016/j.nima.2022.167821). URL: [https : / / doi . org / 10 . 1016 % 5 C % 2 F j . nima . 2022 . 167821](https://doi.org/10.1016%5C%2Fj.nima.2022.167821).
- [43] Sara Ruiz Daza. "Monte Carlo Simulations of Detector Prototypes Designed in a 65 nm CMOS Imaging Process". Presented 25 Nov 2022. 2022.
- [44] H. Wennlöf. *Private Communication*. Jan. 2023.

Appendices

Appendix A

Bethe-Bloch Formula

The Bethe-Bloch formula reproduced in Equation 2.2, provides the mean energy loss along the trajectory's path for incoming heavy particles ($m \gg m_e$) [18].

$$-\left\langle \frac{dE}{dx} \right\rangle = 4\pi N_A r_e^2 m_e c^2 \frac{Z}{A} \rho \frac{z^2}{\beta^2} \left[\frac{1}{2} \ln \frac{2m_e c^2 \beta^2 \gamma^2 T_{max}}{I^2} - \beta^2 - \frac{\delta(\beta\gamma)}{2} - \frac{C(\beta\gamma, I)}{Z} \right] [\text{MeV g}^{-1} \text{cm}^2] \quad (6.1)$$

where

N_A - Avogadro's number (= number of atoms per gram atom)

r_e - classical electron radius

m_e - electron mass

Z, A - atomic number and atomic weight of the absorber

I - mean excitation energy

z, β - charge and velocity of the projectile particle

γ - Lorentz factor

T_{max} - maximum energy transfer in a single collision

$\delta(\beta\gamma)$ - density correction, important for high energies

$C(\beta\gamma, I)/Z$ - the shell correction, relevant for small β values (low energies)

Mobility Model

The Masetti-Canali charge carrier mobility was used in the MC simulations and presented in this thesis as:

$$\mu(E, N) = \frac{\mu_m(N)}{(1 + (\mu_m(N) \cdot E/v_m)^\beta)^{1/\beta}} \quad (6.2)$$

The constant parameters v_m and β , for electrons (e) and holes (h), are [19]:

$$v_{m,e} = 1.53 \times 10^9 \cdot T^{-0.87} \text{ cm s}^{-1}$$

$$\beta_e = 2.57 \times 10^{-2} \cdot T^{0.66}$$

$$v_{m,h} = 1.62 \times 10^8 \cdot T^{-0.52} \text{ cm s}^{-1}$$

$$\beta_h = 0.46 \times 10^{-2} \cdot T^{0.17}$$

Appendix B

Simulation Scripts of TCAD

The following Sentaurus TCAD tools are used:

- SDE: Code will not be made available for this thesis;
- SDevice: Full code at Listing 6.1.

```
1 Device Diode
2 {
3     Electrode
4     {
5         {Name="con_back" voltage=0.0}
6         {Name="con_px_0" voltage=0.0}
7         {Name="con_px_5" voltage=0.0}
8     }
9     File
10    {
11        Grid="n@node|-1@msh.tdr"
12        Current="px_des.plt"
13        Plot="px_des.dat"
14    }
15    Physics
16    {
17        Fermi
18        Temperature = 293
19        Mobility(
20        DopingDependence
21        eHighFieldSaturation
22        hHighFieldSaturation
23    )
24        Recombination(
25        SRH(
26        DopingDependence
27        TempDependence
28    )
29
30        eAvalanche
31        hAvalanche
32
33    )
34        EffectiveIntrinsicDensity (BandGapNarrowing(Slotboom))
35
36    }
37 }
38
```

```
39 System
40 {
41     Diode nnp (
42         "con_back" =bg
43         "con_px_0" =p0_bot
44         "con_px_5" =p5_bot
45     )
46     Vsource_pset v_b (bg 0) {dc = 0}
47     Vsource_pset v_p (p5_bot 0) {dc = 0}
48     Vsource_pset vReset (Reset 0) {dc = 0}
49
50     Resistor_pset r0_bot (p0_bot Reset) {resistance = 10}
51 }
52 File
53 {
54     Output="px_des.log"
55 }
56 Plot
57 {
58     eCurrent/Vector hCurrent/Vector Current/vector
59     eDensity hDensity
60     ElectricField ElectricField/Vector
61     eParallel hParallel
62     Potential SpaceCharge
63     Doping DonorConcentration AcceptorConcentration
64     Auger eAvalanche hAvalanche AvalancheGeneration
65     eMobility hMobility
66     SRHRecombination
67     HeavyIonCharge HeavyIonGeneration
68     eAlphaAvalanche hAlphaAvalanche
69     eTrappedCharge hTrappedCharge
70     eInterfaceTrappedCharge hInterfaceTrappedCharge
71     eGapStatesRecombination hGapStatesRecombination
72
73 }
74 Math
75 {
76     Method= Pardiso
77     Number_of_Threads=48
78     Extrapolate
79     Derivatives
80     RelErrControl
81     Digits=3:
82     Notdamped=15
83     Iterations=10
84     RecBoxIntegr(5e-3 50 5000)
85     Transient = BE
86 }
87 Solve
```

```
88 {
89     Coupled (iterations=100){Poisson}
90     Coupled (iterations=100){Poisson Electron Hole Circuit}
91     NewCurrentPrefix = "./output/pitch_@pitch@/@V_p@/pix_--@V_p@V_"
92     QuasiStationary(
93     InitialStep=1e-7
94     Minstep=1e-50
95     MaxStep=0.01
96     Increment=1.41
97     Decrement=4
98     Goal{
99         Parameter=v_b.dc
100         voltage=-@V_p@
101     }
102     Goal{
103         Parameter=v_p.dc
104         voltage=-@V_p@
105     }
106     Goal
107     {
108     Parameter = vReset.dc
109         Voltage = 1.2
110     }
111
112
113 )
114 {
115     Coupled(iterations=10){Poisson Electron Hole Circuit}
116     Plot (FilePrefix = "./output/pitch_@pitch@/@V_p@_gap@gap_width@/pix_--@V_p@V_" Time = (Range = (0.0
117         1) Intervals = 10) NoOverwrite)
118 }
119 #Plot(NoOverwrite)
120 Save(FilePrefix="./output/pitch_@pitch@/@V_p@_gap@gap_width@/voltage_ramp--@V_p@V_")
121 }
```

Listing 6.1: Geometric model used in the 3D TCAD simulations using the SDE tool.

Appendix C

Simulation Scripts of Allpix²

The simulation flow illustrated in Figure 4.4 contains the following files

- *model.conf*: with the example depicted on Listing 4.2;
- *geometry.conf*: with the example depicted on Listing 4.3;
- *simulation_ETAcalc.conf*: with the example depicted on Listing 6.2;
- *simulation_ETAcorrec.conf*: with the example depicted on Listing 4.14.

```
1 [AllPix]
2 detectors_file = "geometry.conf"
3 model_paths = "model.conf"
4 root_file = "modules_35um.root"
5 multithreading = true
6 random_seed = 24
7 number_of_events = 500000
8
9 [GeometryBuilderGeant4]
10 world_material = "air"
11
12 [ElectricFieldReader]
13 model = "mesh"
14 file_name = "field_ElectricField.apf"
15 depletion_depth = 10um
16 field_mapping = PIXEL_FULL
17
18 [DopingProfileReader]
19 model = "mesh"
20 file_name = "field_DopingConcentration.apf"
21 depletion_depth = 10um
22 field_mapping = PIXEL_FULL
23
24 [DepositionGeant4]
25 physics_list = QGSP_BERT_EMZ
26 enable_pai = 1
27 particle_type = "e-"
28 number_of_particles = 1
29 source_energy = 5GeV
30 source_position = 0um 0um -10mm
31 source_type = "beam"
32 beam_size = 100um
33 beam_divergence = 0mrad 0mrad
34 beam_direction = 0 0 1
```

```
35 max_step_length = 0.5um
36
37 [GenericPropagation]
38 temperature = 293K
39 mobility_model="masetti_canali"
40 recombination_model = "srh_auger"
41 charge_per_step = 5
42 timestep_min = 0.5ps
43 timestep_max = 0.05ns
44 integration_time = 25ns
45 propagate_electrons = true
46
47 [EtaCalculation]
48 chi2ndof_cut = 100
49 eta_formula_x = [0] + [1]*x + [2]*x^2 + [3]*x^3 + [4]*x^4 + [5]*x^5
50
51 [PulseTransfer]
52 max_depth_distance=0.55um
53 collect_from_implant = true
54
55 [DefaultDigitizer]
56 electronics_noise = 10e
57 threshold = 200e
58 threshold_smearing = 5e
59
60 [DetectorHistogrammer]
61 name = "detector"
62 output_plots = 1
63 track_resolution = 0um 0um
64 granularity = 100, 100
65
66 [ROOTObjectWriter]
67 file_name = "data.root"
```

Listing 6.2: simulation_ETAcalf.conf.